High Capacity Fiber-Connected Wireless MIMO Communication

Husileng Bao

Abstract

There will be more and more users while beyond-5G (B5G) and 6G bring more wireless applications. Current cellular communication networks assign specific serving boundaries for each radio, which becomes a limitation when too many users work with one radio simultaneously. By physically distributing radios. user's service can be more uniform. Radio-over-fiber is a promising enabling technology for distributed antenna systems.

To have several tens of Gbit/s data rate, we need to apply millimeter-wave (mm-wave) frequency band in radio-over-fiber (RoF). However, mm-wave signals have weak penetration and high propagation loss. Hence, beamforming and/or multiple-input-multiple-output (MIMO) technology become necessary for mm-wave RoF to overcome those drawbacks.

This thesis introduces an automatic distributed MIMO (D-MIMO) testbed with a statistical MIMO capacity analysis for an indoor use case. Raytracing-based simulations also predicts the indoor case to make a comparison. The statistical MIMO capacity analysis shows that D-MIMO has a higher and more uniform capacity than co-located MIMO (C-MIMO) in measurements and simulations.

Next, a mm-wave sigma-delta-over-fiber (SDoF) link architecture is proposed for MIMO applications. In the implementation of this link, a QSFP28 fiber link connects a central unit with a remote radio unit with four bandpass sigma-delta-modulation (BPSDM) bitstreams. The remote radio unit generates four mm-wave signals from four BPSDM signals and feeds a linear array antenna. The measurement characterizes the remote radio head at each stage and concludes that this proposed link can reach 800 Msym/s data rate with -0.5 dBm output bandpower.

Furthermore, the proposed link is demonstrated with digital beamforming and multi-user MIMO (MU-MIMO) functionalities. The digital beamforming function reaches 700 Msym/s with -25 dB error vector magnitude (EVM) results by improving the received bandpower in comparison to (single-input-single-output) SISO results. The MU-MIMO function serves two independent users at 500 Msym/s symbol rate and satisfies 3GPP requirements at 1 m over-the-air distance.

In conclusion, this thesis proves that D-MIMO has a higher and more uniform capacity than C-MIMO by statistical analysis from measurements and simulations. The proposed novel mm-wave SDoF link can pave the way for future D-MIMO applications.

Keywords: Radio-over-Fiber, central unit, remote radio head, multiple-input-multiple-output, millimeter-wave.

Acknowledgments

I received countless help during my journey to this licentiate thesis. As doctoral research is pushing the human knowledge boundary, I could not imagine how I could survive without following people:

My first and most gratitude is to my main supervisor, Professor Christian Fager, for giving guidance, valuable feedback, and resources. Your critical micro-level management makes my research results top-notch. Any of your questions "Why" pushes me to pursue the nature of science. Since I started my research three years ago, I finally have the chance to write my most profound thanks in my licentiate thesis, "Thanks! Christian."

Another important person for me is my examiner, Professor Magnus Karlsson, who shapes me as a qualified researcher. Even if we do not often have personal interactions due to where we are located, I know you are always there when I need to talk with someone.

I can not forget you, my industry supervisor, Dr. Filippo Ponzini. Thanks for your creative feedback and supervision. It is always a pleasure to have a pleasant and innovative discussion with you!

I finished most of my courses and research work in the microwave electronic laboratory (MEL) with the help of my colleagues. When I am stuck with my homework, I know there is always someone who can help. When I panic about my measurement, I still can find the necessary support. Please accept my huge thanks, MEL friends!

I had an unforgettable period in Ericsson Research (Pisa, Italy) with my lovely colleagues. You are always giving me top priority for my laboratory activity. I have felt the warmest time from your host. You spoiled me with Italian lunch and coffee, which I can not find anywhere else.

I only feel this section is too short of expressing my gratitude to all of you one by one. "Thank you!"

Husileng Bao
Pisa, December 2022

List of Publications

This thesis is based on the following papers:

[A] **H. Bao**, I. C. Sezgin, Z. S. He, T. Eriksson and C. Fager, *"Automatic Distributed MIMO Testbed for Beyond 5G Communication Experiments,"* 2021 IEEE MTT-S International Microwave Symposium (IMS), 2021.

[B] C. Fager, S. Rimborg, E. Rådahl, **H. Bao**, and T. Eriksson, *"Comparison of Co-located and Distributed MIMO for Indoor Wireless Communication,"* 2022 IEEE Radio and Wireless Symposium (RWS), 2022.

[C] **H. Bao**, Z. S. He, F. Ponzini, and C. Fager, *"Demonstration of Flexible mmWave Digital Beamforming Transmitter using Sigma-Delta Radio-Over-Fiber Link,"* in 2022 52th European Microwave Conference (EuMC), 2022.

[D] **H. Bao**, F. Ponzini, and C. Fager, *"Flexible mm-Wave Sigma-Delta-over-Fiber MIMO Link,"* Submitted for Journal of Lightwave Technology, October, 2022.

The content of the following publications partially overlaps with the appended papers or is out of the scope of this thesis.

[E] **H. Bao**, A. Ziemann and Z. S. He, *"Design and Measurements of MSK-LFM RadCom System,"* 2020 17th European Radar Conference (EuRAD), 2021.

[F] M. F. Keskin, I. C. Sezgin, **H. Bao**, H. Wymeersch and C. Fager, "Localization With Distributed MIMO Using a High-Speed Sigma-Delta-Over-Fiber Testbed," in IEEE Microwave and Wireless Components Letters, vol. 32, no. 7, pp. 923-926, July 2022.

[G] Meyer E, Kruglov D, Krivic M et al, *"The state of the art in beyond 5G distributed massive multiple-input multiple-output communication system solutions,"* Open Res Europe 2022.

Acronyms

3D	Three Dimensional
3GPP	The 3rd Generation Partnership
4G	Fourth Generation
5G	Fifth Generation
64-QAM	64-Quadrature Amplitude Modulation
6G	Sixth Generation
ACPR	Adjacent Channel Power Ratio
ARoF	Analog Radio-over-Fiber
BER	Bit Error Rate
BPF	Bandpass Filter
BPSDM	Bandpass Sigma-Delta Modulation
C-MIMO	Co-located Multiple-Input-Multiple-Output
C-RAN	Centralized Radio Access Network
CDR	Clock Data Recovery
CPRI	Common Public Radio Interface
CU	Central Unit
D-MIMO	Distributed Multiple-Input-Multiple-Output
DAC	Digital-to-Analog Converter
DEMUX	Demultiplexer
DL	Downlink
DRoF	Digital Radio-over-Fiber
DSP	Digital Signal Processing
E/O	Electrical/Optical
eCPRI	Enhanced CPRI
FDD	Frequency Division Duplex
FEC	Forward Error Correction
FPGA	Field Programmable Gate Array
GPS	Global Positioning System
IoT	Internet of Things
LNA	Low Noise Amplifier
LS	Least-Square
LTE	Long-Term Evolution
LuMaMi	Lund University massive MIMO
MCF	Multi Core Fiber
MIMO	Multiple-Input-Multiple-Output

MISO	Multiple-Input-Single-Output
mm-wave	Millimeter Wave
MMSE	Minimum-Mean Squared Error
MRT	Maximum Ratio Transmission
MZM	Mach-Zehnder Modulator
NMSE	Normalized Mean Square Error
O/E	Optical/Electrical
OFDM	Orthogonal Frequency-Division Multiplexing
OTA	Over-The-Air
PA	Power Amplifier
PC	Personal Computer
PLL	Phase-Locked Loop
QSFP28	Quad Small Form-Factor Pluggable 28
RAN	Radio Access Network
RF	Radio Frequency
RoF	Radio-over-Fiber
RRH	Remote Radio Head
RX	Receiver
SDM	Sigma-Delta Modulation
SDoF	Signal-Delta-over-Fiber
SDRs	Software Defined Radios
SISO	Single-Input-Single-Output
SMF	Single Mode Fiber
SNR	Signal-to-Noise Ratio
TDD	Time Division Duplex
TX	Transmitter
UL	Uplink
ZF	Zero-Forcing

Contents

Chapter 1

Introduction

1.1 Motivation

The fifth generation (5G) communication network introduces enhanced Mobile Broadband, Ultra-Reliable and Low Latency Communications, massive Machine-Type Communications, and other applications at tens of Gbit/s data rates [2][3]. Meanwhile, the Internet of things (IoT) will reach millions of devices per square kilometer, and such device density reaches high data rates [4]. Hence, wireless communication systems need to provide higher capacity solutions as user densities increase in 5G and IoT [5][6].

Recently Ericsson reports mobile user subscriptions, 5G subscriptions, and monthly data traffic per user [1], as shown in Figure 1.1. All subscriptions are summarized for 2018 - 2021 and are predicted to be more than 9000 million by the end of 2027 with a steady increase. Since 5G was initially deployed in 2019, the 5G subscriptions are growing aggressively and will be around 4400 million by 2027. Around 2027, the 5G subscriptions will be almost half of all subscriptions, which means 5G will be the dominant communication network in the near future. The mobile data traffic per device per month was 11.9 GB/month in 2021, which is forecast to reach 40 GB/month. This tremendous data traffic and 5G devices are an
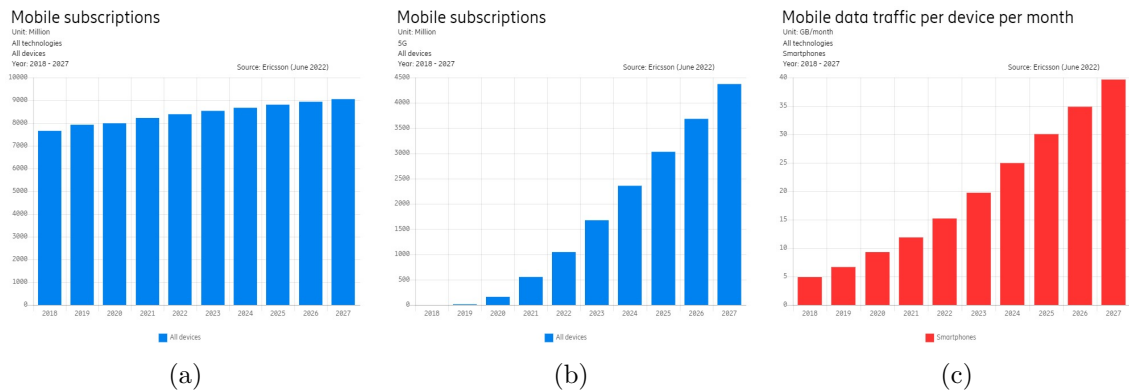

Figure 1.1: Ericsson worldwide study results [1]. (a) User subscriptions; (b) 5G subscriptions; (c) Monthly data traffic per user.

urgent requirement for high capacity wireless communication systems.

Commercial 5G is now available in more than 1300 cities in 61 countries worldwide [7]. On the other hand, the sixth generation (6G) communication network is at the fundamental research stage and aims for a higher capacity, lower latency, higher reliability, and high-density communication strategy by 2030 [8]. Another exciting goal of 6G is low power consumption while allowing anything to communicate anywhere and anytime [9]. For the 6G ambitions, many research institutions and universities have taken action. Ericsson Research expanded the 6G research unit in Britain and predicts new ways of seamless communications [10]. Nokia Bell Labs has 5G and 6G research being developed in parallel, while 6G technology research is in the exploratory start-up phase [11]. Eindhoven University of Technology organized a center for wireless technology from collaborations with five research groups and covers the study of future communication networks [12]. University of Oulu hosts a 6G Flagship Center as the world's first 6G research program towards sustainable solutions for society's needs [13]. In short, 6G is coming as a sustainable ultra-high data rate communication network.

The dramatic increase in 5G subscriptions and 5G commercial network deployments prove that high capacity communication network is a solid requirement a solid requirement in societies. The ultra-high data rate communication system is a hot research topic as 6G research is being developed in world-leading wireless communication research groups.

Research work [14] introduced massive co-located multiple-input-multiple-output (C-MIMO) as a key technology to increase communication capacity in 5G applications. Furthermore, distributed MIMO (D-MIMO) and cell-free (MIMO) have recently been proposed to further improve communication capacity and user service uniformity for 6G [15]. Radio-over-fiber (RoF) has been proposed as a key technology for realization of D-MIMO systems. The RoF testbeds of [16] [17] are D-MIMO implementations as well as fiber-connected wireless systems.

Therefore, this thesis addresses the high capacity fiber connected wireless MIMO communication system as one potential key technology to support the development of future sustainable, high density communication networks.

1.2   Thesis Scope and Outline

Chapter 2 describes the MIMO technology evolution. An overview of different fiber-connected wireless system architectures is also presented in Chapter 2 for D-MIMO implementations, as well as the underlying theories.

Chapter 3 studies the capacity of the proposed fiber-connected D-MIMO system through extensive measurements and simulations. The chapter starts with a summary of the current low-frequency C-MIMO/D-MIMO testbed. The most important contribution is the statistical D-MIMO and C-MIMO study in an indoor environment through an automated testbed in paper [A], and the study concludes that D-MIMO has a more uniform/higher communication capacity than C-MIMO. Paper [B] strengthens the contribution by a comparison between simulation and measurement.

Chapter 4 focuses on millimeter wave (mm-wave) sigma-delta-over-fiber (SDoF) systems and discusses the available solutions. Paper [C] proposes a wideband, flexible, and simple all-digital mm-wave architecture and implements the architecture with commercially available hardware. Chapter 4 also includes an over-the-air (OTA) demonstration of the proposed link and compares the results with state-of-the-art results as in paper [D]. The demonstration of the proposed architecture documents the highest data rate reported so far in any of mm-wave SDoF MIMO system.

The final chapter summarizes the current work and proposes relevant future research topics.

Chapter 2

Wireless MIMO Technology Evolution

The electromagnetic spectrum is extremely crowded in the low-frequency band (up to 6 GHz) with countless applications, for example from business and consumer terminals, and the dense spectrum makes spectral efficiency extremely important. One of the most powerful techniques to increase spectral efficiency is to explore spatial multiplexing through multi-antenna MIMO techniques as proposed in [18] and has been further developed since then. Today, MIMO is a key technology in all modern wireless systems, starting from the fourth generation (4G) mobile system but further exploited in 5G and likely even more in the future. The following subsections cover single-input-single-output (SISO)/multiple-input-single-output (MISO)/MIMO fundamentals for wireless MIMO.

Wireless MIMO systems can be categorized into $co-located$ and $distributed$ variants, where RoF technology plays a key role in the practical system implementation.

2.1   SISO Fundamentals

For the SISO fundamentals, this section goes through the SISO model and the SISO capacity.

2.1.1   SISO Model

A wireless communication system has at least one transmitter (TX) and one receiver (RX). An antenna is the final part of the TX side and radiates the signal into the channel, while the RX side receives the radiated signal from the channel by an antenna at the first stage. The TX antenna is the input port for the wireless channel, and the RX antenna is the output port. A wireless communication system with one TX antenna and one RX antenna constitutes a SISO system.

In Figure 2.1, an ideal SISO communication system is presented, having only one coefficient, h, describing the channel between TX and RX. This channel element is a complex value and describes the amplitude and the phase of the received signal as

Figure 2.1: Principal illustration of (a) SISO case; (b) SISO model.

$$y[n] = hx[n] + w[n], \tag{2.1}$$

where $x[n]$ is the discrete signal at time index n from the TX and $y[n]$ is the corresponding received signal at the RX side, as in Figure 2.1b. In reality, the received signal has additive noise $w[n]$ contributed by the system components and the wireless channel.

2.1.2   SISO Capacity

Assuming a Gaussian channel, a SISO communication system has the ideal communication capacity as [19]

$$C = B \log_2 \left(1 + \frac{S}{N}\right) [\text{bit/s}], \tag{2.2}$$

where B is communication bandwidth and $\frac{S}{N}$ is the signal-to-noise ratio (SNR). Ideally, we can increase bandwidth or SNR to have higher capacity. However, there is limited bandwidth in reality, especially in a low-frequency band. Conversely, increasing SNR will only get a logarithmic capacity increase. Hence, the communication link needs MIMO technology to increase system capacity [20].

2.2   MISO Fundamentals

For the MISO fundamentals, this section goes through the MISO model and the MISO precoding.

2.2.1   MISO Model

One TX antenna has a fixed radiation pattern and must have wide coverage/low gain to assist a mobile user. By replacing the single antenna with a phased array antenna, the radiated signal can be concentrated in the desired direction of the user. In other words, a MISO system has an electrically steerable high-gain antenna at the TX side.
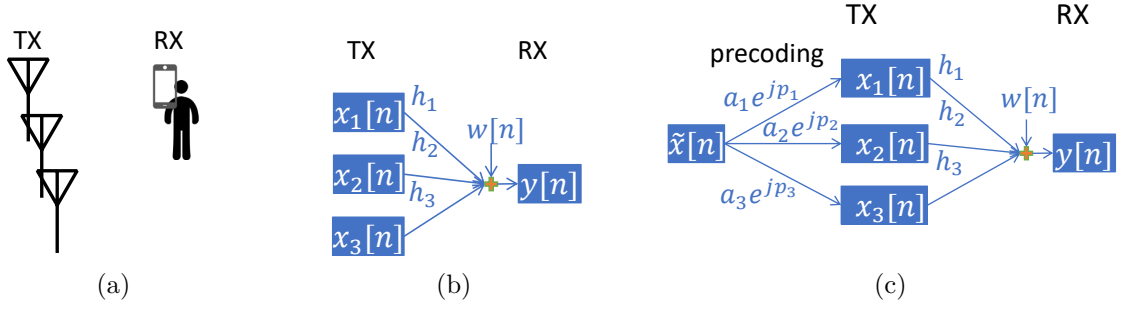
Figure 2.2: Principal illustration of (a) MISO case; (b) MISO model; (c) MISO model with precoding.

Figure 2.2 illustrates a specific case of a 3×1 MISO configuration. Three TX transmit $x_1[n]$, $x_2[n]$, and $x_3[n]$ signals into the communication channel. The channel coefficients h_1, h_2, and h_3 multiply with TX signals, and the RX receives a superimposed signal $y[n]$ given by

$$
\begin{aligned}
y[n] &= h_1 x_1[n] + h_2 x_2[n] + h_3 x_3[n] + w[n] \\
&= \begin{bmatrix} h_1 & h_2 & h_3 \end{bmatrix} \begin{bmatrix} x_1[n] \\ x_2[n] \\ x_3[n] \end{bmatrix} + w[n].
\end{aligned}
\tag{2.3}
$$

This expression can be generalized with precoding to

$$
y[n] = \begin{bmatrix} h_1 & h_2 & h_3 \end{bmatrix} \begin{bmatrix} a_1 e^{jp_1} \\ a_2 e^{jp_2} \\ a_3 e^{jp_3} \end{bmatrix} \tilde{x}[n] + w[n].
\tag{2.4}
$$

where $\tilde{x}[n]$ is a scalar signal to transmit.

The expression of (2.4) is generalized into a $k \times 1$ MISO case as

$$
\begin{aligned}
y[n] &= \begin{bmatrix} h_1 & h_2 & \dots & h_k \end{bmatrix} \begin{bmatrix} a_1 e^{jp_1} \\ a_2 e^{jp_2} \\ \dots \\ a_k e^{jp_k} \end{bmatrix} \tilde{x}[n] + w[n] \\
&= \mathbf{h}^{\mathrm{T}} \mathbf{a} \tilde{x}[n] + w[n].
\end{aligned}
\tag{2.5}
$$

The signals from k antennas superimpose at the RX side with the channel effects. The superimposition can be either constructive or destructive by changing the phases of p_1, p_2, and p_k. The amplitudes of a_1, a_2, and a_k are unity for most cases. The TX changes the amplitudes to decrease the sidelobes in some special cases, which is called amplitude tapering. It is the MISO beamforming function of a $k \times 1$ wireless communication system.

2.2.2   Channel Estimation and Precoding

To estimate the channel coefficients, the TX transmits a pilot signal at first. If the transmitted pilot signal $\mathbf{x}_p$ and the received pilot signal $\mathbf{y}_p$ are known with N samples, a least-square (LS) estimate of the channel information, $\widehat{\mathbf{h}}$, can be expressed as

$$\widehat{\mathbf{h}} = \left(\mathbf{x}_p{}^T \mathbf{x}_p \right)^{-1} \mathbf{x}_p{}^T \mathbf{y}_p. \tag{2.6}$$

The estimated $\widehat{\mathbf{h}}$ can be used for precoding. The Zero-forcing (ZF) precoding starts from Moore–Penrose inverse

$$\mathbf{p} = \left(\widehat{\mathbf{h}} \widehat{\mathbf{h}}^* \right)^{-1} \widehat{\mathbf{h}}. \tag{2.7}$$

For MISO beamforming, there is no multi-user interference in the channels , and TX can radiate maximum power. To maximize the receiver SNR, all TX branches can transmit at the same power. A precoder where only the phase information is kept is therefore optimum

$$\mathbf{p}_{BF} = e^{\mathbf{j}\angle\mathbf{P}}. \tag{2.8}$$

The MISO beamforming expression is

$$\mathbf{x}\left[\mathbf{n}\right] = \mathbf{p}_{BF}^T \tilde{x}\left[n\right]. \tag{2.9}$$

2.3   MIMO Fundamentals

For the MIMO fundamentals, this section goes through the MIMO model, channel matrix decomposition, precoding, and capacity expressions.

2.3.1   MIMO Model

Increasing the TX/RX antennas means increasing the possible independent channels between RX users and TX. Figure 2.3 illustrates the principle of the MIMO technology, in which Figure 2.3a is a single-user case and Figure 2.3b is a multi-user case. Both cases can be modeled in Figure 2.3c where the received signals of y_1 and y_2 are linear combinations of channel elements, RX signals, and additive noises as

$$
\begin{aligned}
\begin{bmatrix} y_1\left[n\right] \\ y_2\left[n\right] \end{bmatrix} &= \begin{bmatrix} h_{11}x_1\left[n\right] + h_{12}x_2\left[n\right] + h_{13}x_3\left[n\right] + w_1\left[n\right] \\ h_{21}x_1\left[n\right] + h_{22}x_2\left[n\right] + h_{23}x_3\left[n\right] + w_2\left[n\right] \end{bmatrix} \\
&= \begin{bmatrix} h_{11} & h_{12} & h_{13} \\ h_{21} & h_{22} & h_{23} \end{bmatrix} \begin{bmatrix} x_1\left[n\right] \\ x_2\left[n\right] \\ x_3\left[n\right] \end{bmatrix} + \begin{bmatrix} w_1\left[n\right] \\ w_2\left[n\right] \end{bmatrix},
\end{aligned} \tag{2.10}
$$

where h_{11}, h_{12}, and h_{13} are channel elements from TX antennas to RX antenna one, while h_{21}, h_{22}, and h_{23} are channel elements from TX antennas to RX antenna two.
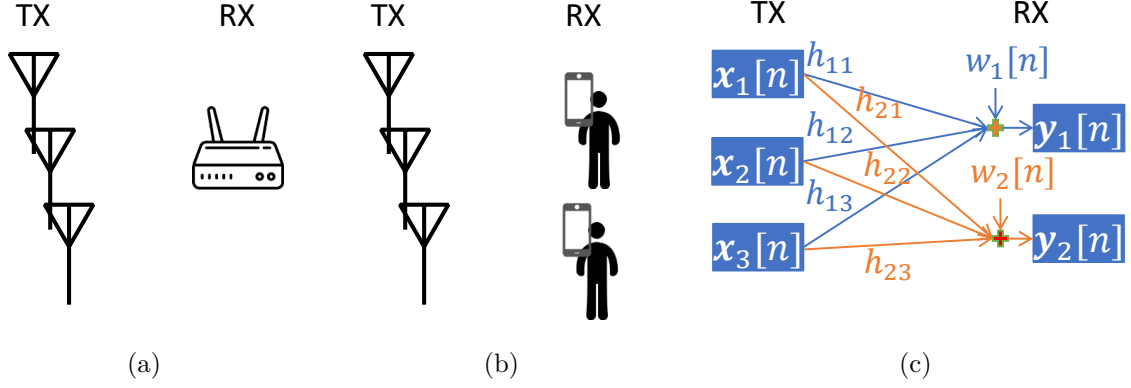
(a) (b) (c)

Figure 2.3: Principal illustration of (a) single-user MIMO case; (b) multi-user MIMO case; (c) general MIMO model.

Three TX signals of x_1, x_2, and x_3. The additive noise contributions are w_1 and w_2 for two RX signals.

In a general $k \times r$ MIMO system, the signal expression becomes

$$\begin{bmatrix} y_1\left[n\right] \\ ... \\ y_r\left[n\right] \end{bmatrix} = \begin{bmatrix} h_{11} & h_{12} & ... & h_{1k} \\ ... & ... & ... & ... \\ h_{r1} & h_{r2} & ... & h_{rk} \end{bmatrix} \begin{bmatrix} x_1\left[n\right] \\ x_2\left[n\right] \\ ... \\ x_k\left[n\right] \end{bmatrix} + \begin{bmatrix} w_1\left[n\right] \\ ... \\ w_r\left[n\right] \end{bmatrix}, \tag{2.11}$$

or in a matrix form

$$\mathbf{y} = \mathbf{H}\mathbf{x} + \mathbf{w}. \tag{2.12}$$

where $\mathbf{x}$ is the transmitted signal with $k \times 1$ dimension, and k is the number of TX antennas. $\mathbf{y}$ is the received signal matrix with $r \times 1$ dimension, and r is the number of RX antennas. $\mathbf{w}$ is a additive channel noise matrix with $r \times 1$ dimension.

2.3.2 Channel Matrix Decomposition

The singular value decomposition of a $r \times k$ complex matrix $\mathbf{H}$ is

$$\mathbf{H} = \mathbf{U}\mathbf{\Sigma}\mathbf{V}^*$$
$$= \begin{bmatrix} u_{11} & u_{12} & ... & u_{1r} \\ u_{21} & u_{22} & ... & u_{2r} \\ ... & ... & ... & ... \\ u_{r1} & u_{r2} & ... & u_{rr} \end{bmatrix} \begin{bmatrix} \sigma_{11} & 0 & ... & 0 \\ 0 & ... & ... & 0 \\ ... & ... & \sigma_{ii} & ... \\ 0 & 0 & ... & ... \end{bmatrix} \begin{bmatrix} v_{11} & v_{12} & ... & v_{1k} \\ v_{21} & v_{22} & ... & v_{2k} \\ ... & ... & ... & ... \\ v_{k1} & v_{k2} & ... & v_{kk} \end{bmatrix}^*, \tag{2.13}$$

where $\mathbf{U}$ is a $r \times r$ complex unitary matrix, $\mathbf{\Sigma}$ is a $r \times k$ rectangular diagonal matrix with non-negative real numbers on the diagonal, $\mathbf{V}$ is a $k \times k$ complex unitary matrix, and $\mathbf{V}^*$ is the conjugate transpose of $\mathbf{V}$. Such decomposition exists for any complex matrix. The matrices $\mathbf{U}$ and $\mathbf{V}$ have the property that $\mathbf{U}^* = \mathbf{U}^{-1}$ and $\mathbf{V}^* = \mathbf{V}^{-1}$, which means the conjugate transpose is the same as the inverse. The
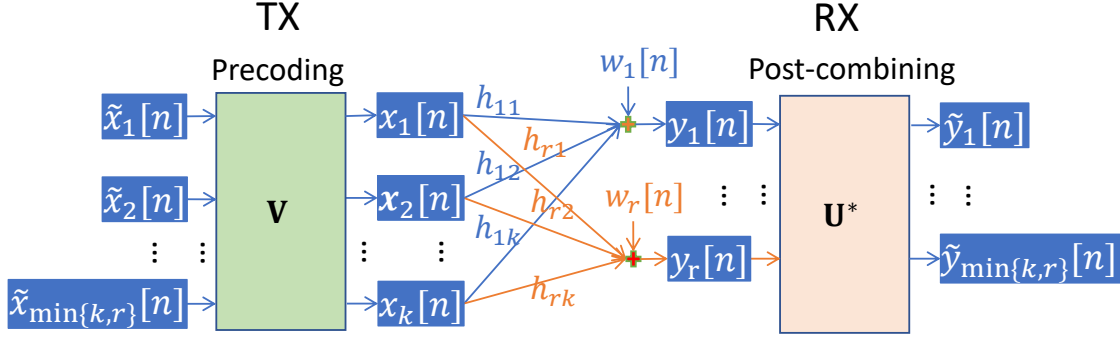
Figure 2.4: The MIMO model with precoding and post-combining.

diagonal entries σ_{ii} of $\mathbf{\Sigma}$ are uniquely determined by $\mathbf{H}$ and are known as the singular values of $\mathbf{H}$. The number of non-zero singular values is equal to the rank of $\mathbf{H}$. The rank is also the number of independent sub-channels that the MIMO system ideally can support [21].

Figure 2.4 explains precoding and post-combining based on the matrix $\mathbf{V}$ and $\mathbf{U}^*$. The resulting independent MIMO channels are given by

$$\begin{cases} \tilde{\mathbf{y}} = \mathbf{U}^*\mathbf{y} \\ \tilde{\mathbf{x}} = \mathbf{V}^*\mathbf{x} \\ \tilde{\mathbf{w}} = \mathbf{U}^*\mathbf{w}. \end{cases} \tag{2.14}$$

The resulting channel model is

$$\tilde{\mathbf{y}} = \mathbf{\Sigma}\tilde{\mathbf{x}} + \tilde{\mathbf{w}}. \tag{2.15}$$

2.3.3   Channel Estimation and Precoding

Channel estimation is the process of estimating the channel matrix, $\mathbf{H}$. The LS principle [22] minimizes the channel estimation errors [20]. The channel matrix is then used for precoding. With the transmitted pilot signals $\mathbf{X}_\text{p}$ and the received pilot signals $\mathbf{Y}_\text{p}$, the LS algorithm calculates the channel information $\widehat{\mathbf{H}}$ as

$$\widehat{\mathbf{H}} = \left(\mathbf{X}_\text{p}{}^\text{T}\mathbf{X}_\text{p}\right)^{-1}\mathbf{X}_\text{p}{}^\text{T}\mathbf{Y}_\text{p}. \tag{2.16}$$

In MU-MIMO, there is no post-combining in the RX since they cannot collaborate, and this section only explains the precoding at the TX. The ZF precoding, which is commonly used, is designed to minimize the multi-user interference for MIMO communication. The ZF MIMO precoder is derived from the Moore–Penrose inverse of the estimated channel matrix as

$$\mathbf{P} = \left(\widehat{\mathbf{H}}\widehat{\mathbf{H}}^*\right)^{-1}\widehat{\mathbf{H}}. \tag{2.17}$$

The ZF precoding of user data $\tilde{\mathbf{x}}$ is done according to

$$\mathbf{x} = \mathbf{P}^\text{T}\tilde{\mathbf{x}}. \tag{2.18}$$

Maximum ratio transmission (MRT) precoding maximizes signal power for RX users by conjugate matching with channel matrix. MRT is also referred to as a matched filter or conjugate beamforming since MRT precoding is a multiplication of conjugate transpose of estimated channel information and user data as

$$\mathbf{x} = \widehat{\mathbf{H}}^* \tilde{\mathbf{x}}. \tag{2.19}$$

2.3.4   Capacity Expressions

MIMO introduces spatial diversity for wireless systems, thereby increasing the channel capacity using channel information and exploiting parallel channels. The sum MIMO capacity is from [23] as

$$C_{MIMO} = \sum_{m=1}^{M} B \log_2 \left(1 + \sigma_m^2 \frac{S}{N} \right) [\text{bit/s}], \tag{2.20}$$

where C_{MIMO} is the sum MIMO capacity and σ_m^2 is the channel weight. Equation (2.20) is based on the assumption of identical $\frac{S}{N}$ for all channels. M is the number of independent channels and is decided by the rank of $\mathbf{H}$. In theory, increasing the channel number can increase MIMO capacity linearly. However, the actual MIMO capacity also depends on non-line-of-sight conditions and interference [24]. Only simulations are not enough to ultimately show the MIMO system's ability. The following sections will go through MIMO testbeds and study the capacity of MIMO cases by experiment and simulation.

2.4   Wireless MIMO Technology

MIMO technology in wireless communication improves the capacity as described in the previous section. A critical prerequisite for MIMO technology is phase coherence between TXs. In this section, C-MIMO, D-MIMO, and cell-free MIMO architectures are described.

2.4.1   Co-located MIMO

The conventional and intuitive MIMO implementation is the C-MIMO method. C-MIMO has multiple closely located antennas at the TX side and transmits signals for multiple RX users. The C-MIMO communication system applies an array antenna, for instance in the form of linear array antenna, planar array antenna, or circular array antenna, which contributes to increased antenna gain and improved signal SNR. The users are coherently served by all the antennas, in the same time-frequency resources but separated in the spatial domain by receiving very directive and different signals.

However, C-MIMO has some drawbacks in reality. The user-interference is becoming the major bottleneck as we densify the users. It cannot be removed as long as we rely on co-located implementations [14]. In Figure 2.5a, the TX (as a C-MIMO) serves two users simultaneously. The TX signals are too close and coupled
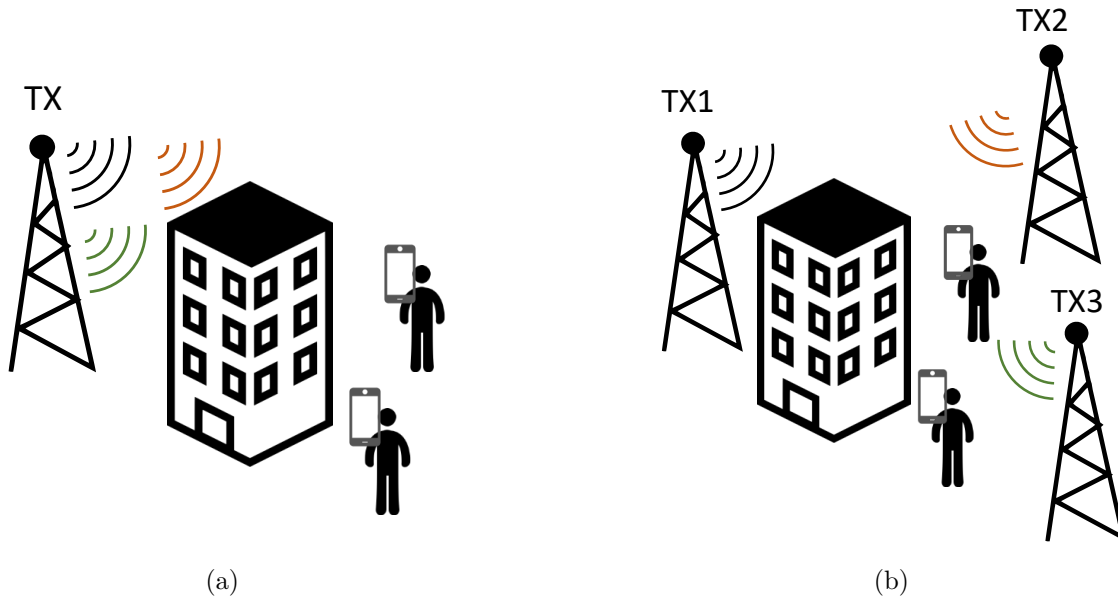
<center>(a)</center>

<center>(b)</center>

Figure 2.5: A specific case of (a) C-MIMO can not reach users due to blockage. (b) D-MIMO has a better possibility to cover users irrespective of their location .

with each other. From each user's perspective, the TX antennas do not show enough channel diversity. The signals that the users receive from different antennas are too similar, which means that adding another antenna does not add much protection against fading dips and outages. For a high-frequency band, a single building can block any users and degrades the signal quality, as shown in Figure 2.5a.

2.4.2   Distributed MIMO

When payments, navigation, entertainment, and control of autonomous vehicles are all relying on wireless connectivity, we must raise the uniformity of the data service quality. With the increased peak data rates, the more important is that rates can be guaranteed to the vast majority of the locations in the geographical coverage area [25]. This leads to the D-MIMO communication system which has multiple distributed TXs. Physically distributed antennas with different TX do not have signal coupling problems and are more likely to have line-of-sight communication with RX. Figure 2.5b is a specific D-MIMO technology illustration with three distributed TXs serving the users. The high-density urban area can have a uniform service from such a distributed system. Dense deployment of D-MIMO systems can lead to the important communication system concept, cell-free MIMO, to be discussed in the next subsection.

For the wireless communication technologies mentioned above, the MIMO antennas need coherent transmitters that generate wireless signals. The phase coherence requirement is one big challenging factor for D-MIMO implementations. Sections 2.5 and 2.6 cover the MIMO implementation and the RoF architectures for the MIMO technologies.
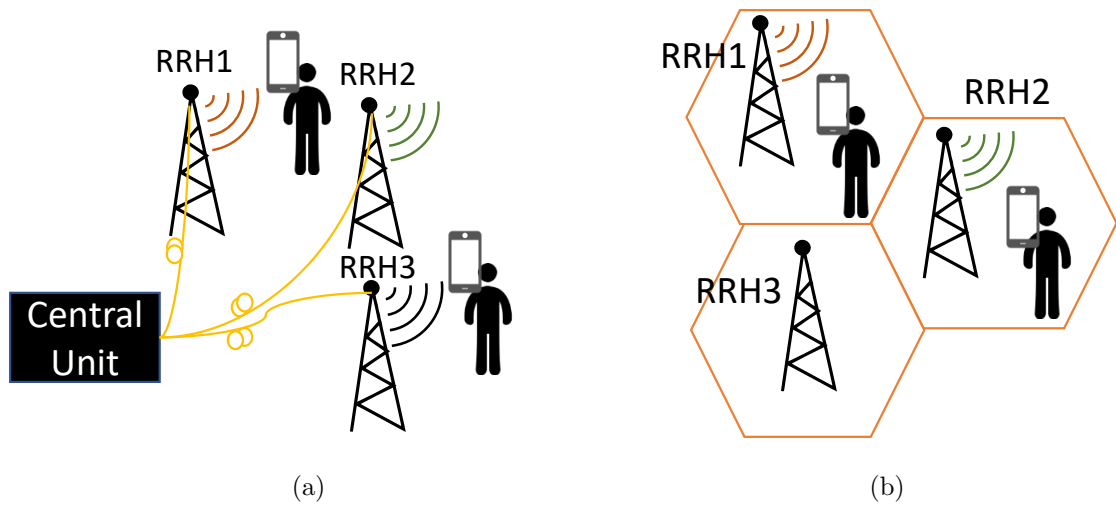
(a)   (b)

Figure 2.6: (a) The cell-free system is user-centralized. (b) The cellular system has an unbalanced load.

2.4.3   Cell-free MIMO

The word "cell-free" signifies that there are no cell boundaries during data transmission, but all (or a subset of) remote radio heads (RRHs) in the network cooperate to serve the users in a user-centric fashion jointly [26]. The RRHs are connected via fronthaul connections to the central unit (CU), which is responsible for the coordination as Figure 2.6a shows. Figure 2.6 compares a cellular MIMO with a cell-free MIMO. A cell-free system can serve users dynamically without specific serving area definitions and suggests a user-friendly communication system. In the cell-free of Figure 2.6a, the service's load is balanced by the three RRHs equally.

In contrast, in a cellular communication system, each RRH has a specific serving area with a boundary and only connects with users in that area. An important fact is that signal power rapidly decays with the propagation distance. The user that happens to be close to an RRH (i.e., in the cell center) will experience a higher SNR than those that are close to the edge between two cells. A 10000 times (40 dB) difference is common between the cell center and cell edge [26]. Moreover, users at the cell edge are also affected by interference from neighboring RRHs [25]. For mobile communication systems, the users can move around the cell edge and might be traveling cell boundaries back and forth. The cells must release and frequently schedule all resources for such cell edge users. In the end, the cellular communication system has a nonuniform service. A specific example is in Figure 2.6b. While RRH1 and RRH2 are busy, RRH3 is free due to cellular system-defined boundaries.

2.5   Wireless MIMO Transmitter Implementations

This section covers the TX implementations for wireless C-MIMO/D-MIMO technologies.
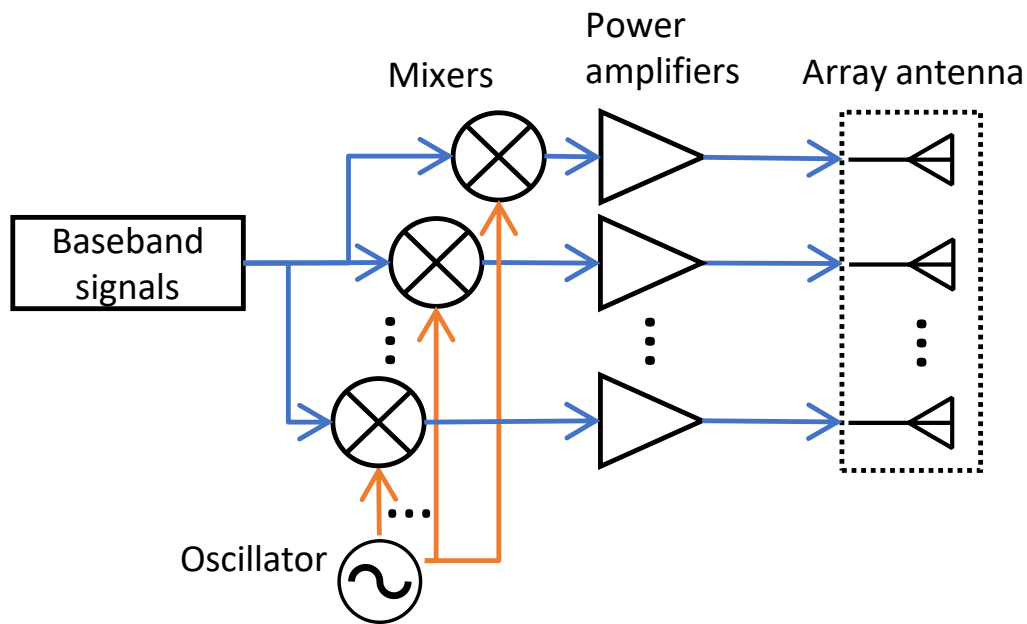
Figure 2.7: The general transmitter structure for C-MIMO implementations.
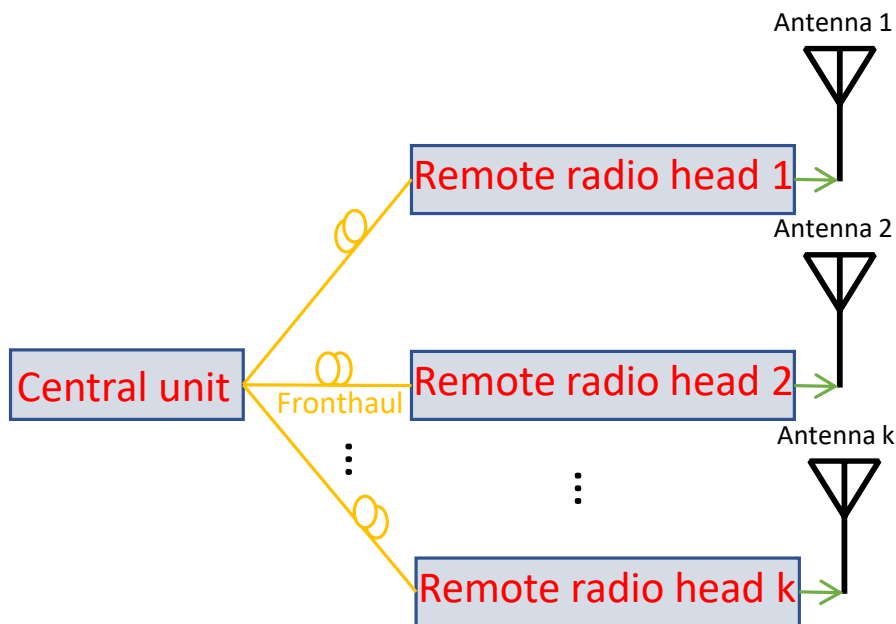
Figure 2.8: The D-MIMO transmitter implementation illustration.

2.5.1   Co-located MIMO Implementations

In C-MIMO implementations, all antennas, electronics and signal processing compo-
nents needed for MIMO communication are placed in the same unit. The critical
thing is that the branches can use the same local oscillator, and it is much easier to
maintain phase coherence between the channels, which is a prerequisite for MIMO.

There are several branches of a power amplifier (PA), a mixer for an array antenna
in C-MIMO implementations, as shown in Figure 2.7. The input baseband signal is

upconverted by the mixer and the oscillator to a radio frequency signal. The TX also needs filters to suppress unwanted spectrum and keeps target frequency. For specific applications, the structure needs to be modified. A high-frequency communication system might need upconversions at several stages. An amplifier stage could be needed before the mixer if the baseband signal is weak. In a word, TXs generate radio frequency signals with sufficient power to the array antenna.

2.5.2 Distributed MIMO Implementations

D-MIMO requires the transmitters to be physically and remotely distributed to introduce channel diversity. The fronthaul connection separates the CU and the RRH, as in Figure 2.8. This way, the CU implements the central processing of MIMO technology for the distributed RRHs and simplifies the RRH. The fronthaul connection is also responsible for keeping coherence signals for remote radios as MIMO technology required.

2.6 Radio-over-Fiber Technology

For the D-MIMO implementations, RoF technology is commonly used for this purpose. The RoF technology can have several architectures, which are described in this section.

2.6.1 Architecture

Optical fiber is low-cost material with low attenuation of optical signals in the order of 0.2 dB/km. Moreover, fiber-connected wireless communication structure allows the RRH to be deployed remotely at several kilometers of distance. The RoF architectures are already a mature technology in 4G and 5G radio access network (RAN) deployments [27] [28].

For a low-frequency (sub-6 GHz) band, RoF architectures are classified into analog radio-over-fiber (ARoF), digital radio-over-fiber (DRoF) [29], [30], and SDoF [16], [17], [31], generally as in Figure 2.9. The modern CU has a digital signal processing (DSP) unit for baseband signal processing. ARoF generates an analog radio frequency (RF) signal from the digital-to-analog converter (DAC) and transmits it to the RRH through a fiber, as shown in Figure 2.9a. ARoF only needs a PA to amplify the analog RF signal from the fiber connection. Even if the ARoF can have such a simple RRH, the optical signal may cause distortion due to impairments in the optical components [32] [33].

In Figure 2.9b, the DRoF structure shifts the DAC to the RRH and transmits digitized RF signals through the fiber connection. Since the digital signal only has zeros and ones, the optical signal does not have any significant distortion problem. However, the signal from the optical/electrical (O/E) converter can not be connected to the DAC directly because of the different signal protocols between the optical signal and the DAC signal requirements [29]. There is usually a DSP unit that is a signal protocol agency between the O/E and the DAC in the RRH [30]. This
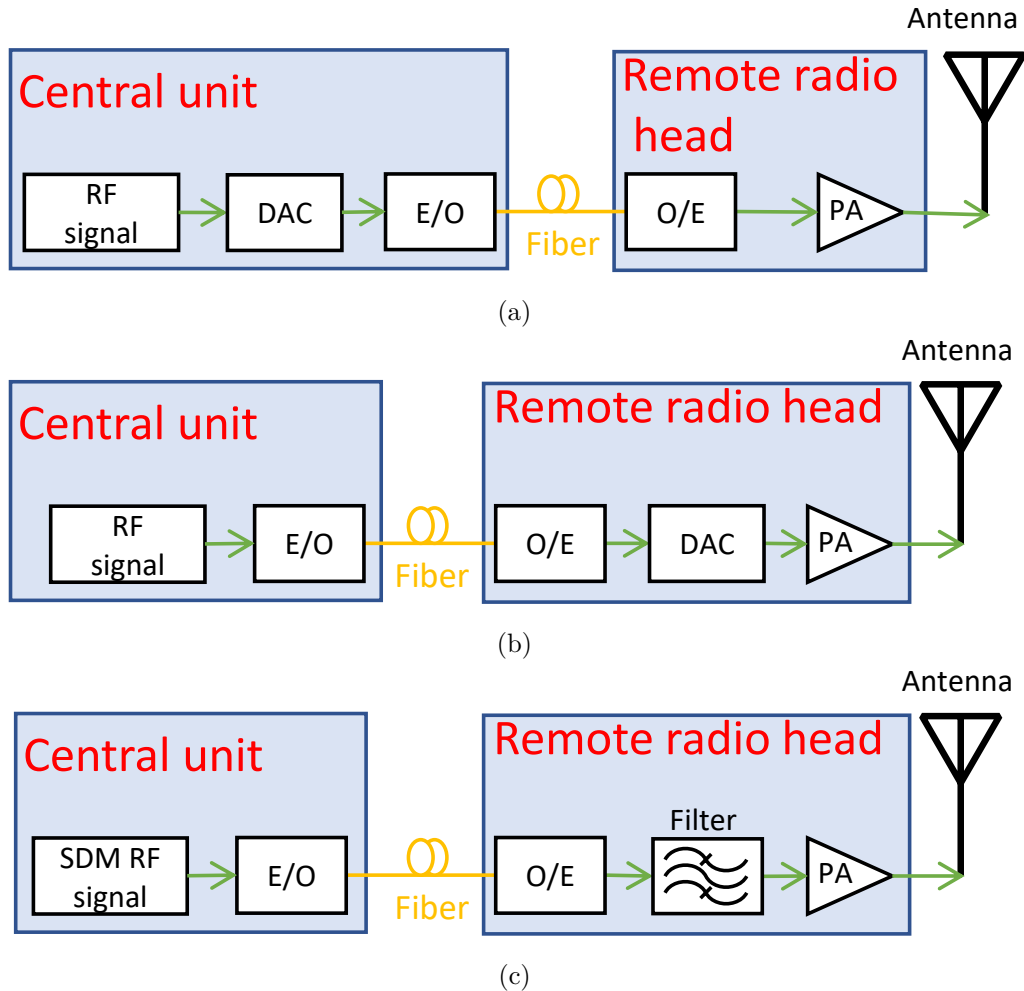
Figure 2.9: The principle illustration of (a) Analog Radio-over-Fiber. (b) Digital Radio-over-Fiber. (c) Sigma-Delta-over-Fiber .

DSP requirement makes the DRoF structure more complicated and not an optimum choice for massive MIMO deployment. A high-speed DAC is usually really expensive and hard to design. Therefore, the DAC is another limitation in the ARoF and DRoF structure.

Some studies introduce SDoF architecture with simple RRH which overcomes the problem of the previous architectures [16], [17], [31]. In Figure 2.9c, the CU applies bandpass sigma-delta modulation (SDM) with a digital RF signal to generate bit-streams for fiber connection, and the RRH only needs a bandpass filter (BPF) to recover the analog RF signal. Therefore, the SDoF structure does not need an expensive DAC and has a high tolerance for the optical signal. Chapter 3 will go through low-frequency specific RoF testbeds with these architectures.

The RoF architectures mentioned above need improvements for the mm-wave band (above 24 GHz). For example, the RoF architectures need to generate a mm-wave signal at CU or RRH [34]. Meanwhile, the fiber connection must also be capable of broad bandwidth signals. Chapter 4 will introduce such mm-wave RoF systems.

2.6.2 MIMO Applications

In current 4G and 5G systems, the centralized radio access network (C-RAN) implementation is a centralized system [35]. The C-RAN communication system keeps intensive computations in a CU and allows simple RRHs [4]. Such a centralized network, C-RAN, can have a high capacity from the MIMO function [36], which requires coherent RRHs. Based on previous architecture discussions, the RoF MIMO system can share synchronized signals from the CU by a fiber connection. However, DRoF has the most complicated RRH and is therefore not an attractive solution for MIMO systems. Chapter 3 covers the current RoF D-MIMO systems, including ARoF, DRoF, and SDoF structures.

2.7 Chapter Conclusion

This chapter has summarized the system model and the capacity for SISO/MISO/MIMO technologies theoretically. In wireless MIMO communication, the D-MIMO technology forms a basis for the cell-free MIMO system concept. In the end, the wireless MIMO implementations address different architectures in terms of pros and cons.

Chapter 3

Experimental Evaluation of Wireless MIMO Systems

MIMO technology improves channel capacity in wireless communication systems for increasing users, as discussed in Chapter 2. This chapter reviews the current testbeds for experimentally statistically exploring MIMO capacity in realistic environments. MIMO simulations are also important to be included as a comparison of the experimental results.

3.1   Communication Testbeds

The theoretical ideas and mathematical simulation always simplify noise and propagation parameters in a real environment full of multipath. Hence, the MIMO study needs a proof-of-concept prototyping system to verify real MIMO communication performance. This section addresses MIMO testbeds from academia and industry in C-MIMO and D-MIMO categories.

3.1.1   C-MIMO Communication Testbeds

In 2014, with the collaboration of the University of Bristol, Lund University massive MIMO (LuMaMi) was reported with a real-time digital transceiver chain [37]. LuMaMi has a 'T' shaped array antenna with 160 dual-polarized elements and can support 4×25 and 10×10 configurations. In the testbed platform, the upper part of the 'T' shape, with 4×25 elements, connects with 50 software-defined radios (SDRs), each of them has two independent RF transceivers. These radios work with 20 MHz bandwidths at 3.7 GHz carrier frequency and are connected to a central processor through switch combiners. The central processor deals with real-time uplink (UL)/downlink (DL) 384 Gbps data. With the engineering improvements, some of the real-time baseband signal processing is shifted to the SDRs, and the total data rate is reduced for switch combiners as the latency time is also dropped. All components are off-the-shelf hardware equipped on a trolley to have mobility for measurements. LuMaMi has indoor and outdoor measurements serving 12 simultaneously active users with ZF and MRT precoding at time division duplex (TDD) mode [38]. The

measurement results showed that it is possible to separate up to 12 user equipments on the same time/frequency resource when using massive MIMO. LuMaMi is also able to communicate with moving cars at 29 km/h velocity by updating the channel state information and the power control [39]. During measurements, 100 RF signals are synchronized and coherent by a standard distributed reference clock and timing trigger at the base station. Receivers are synchronized to global positioning system (GPS) reference and primary synchronization signal of orthogonal frequency-division multiplexing (OFDM) symbols.

EURECOM, a French research center in Sophia Antipolis, has the OpenAirInterface massive MIMO testbed, an open-source long-term evolution (LTE) compliant base station. equipped with array antenna [40]. It has an array antenna with 64 elements and works at 2.6 GHz carrier frequency with 5 MHz bandwidth. Four commercial user terminals connect with the internet service simultaneously through this massive MIMO testbed at TDD mode [40].

Despite these academic testbeds above, there are also C-MIMO research results or products from industry. A proof-of-concept base-station prototype reached a full-dimension MIMO technology at Samsung Research [41]. An array antenna with 8×4 dual-polarized patch elements connects 32 transceivers, followed by a baseband board. During the indoor/outdoor measurements, 12 user terminals get real-time LTE service at 3.5 GHz carrier frequency with 20 MHz bandwidth by sharing same time/frequency resources [41]. Ericsson has a wideband MIMO product of AIR 6428, which has 64 transceivers for 192 antenna elements [42]. AIR 6428 supports 400 MHz instantaneous bandwidth at sub 6-GHz frequency band [42]. Ericsson introduces 2×1, 4×1, and 8×1 sub-array MIMO configurations for dense urban high-rise, urban low-rise, and rural areas respectively [43]. At the same time, Nokia's AirScale massive MIMO Adaptive Antenna also has 64 transceivers and made a joint beamforming demonstration with a U.S. operator at Mobile World Congress in Barcelona, Spain [44].

3.1.2 D-MIMO Communication Testbeds

Katholieke Universiteit Leuven (Belgium) first analyzed the infrastructure sharing spectrum efficiency with a D-MIMO testbed [45] for an outdoor environment. This Leuven D-MIMO testbed has two base stations (or RRHs), each based on the MIMO testbed in [46] and has an array antenna with 32 patch elements. All antenna elements have independent RF signals from SDRs and radiate 20 MHz LTE signal at 2.6 GHz carrier frequency with TDD mode. The outdoor measurement results conclude that D-MIMO configuration significantly increases spectrum efficiency with minimum-mean squared error (MMSE) precoding. Furthermore, the Leuven D-MIMO testbed tackled the inter-user interference problem in an indoor experiment [47]. Some researchers propose a new RAN concept of RadioWeaves [48] based on the Leuven D-MIMO testbed. The measurements in [49] validate the advantages of RadioWeaves (planar distributed) topology by comparing it with Ericsson's RadioStripes (linear distributed topology) [50].

Recently, Samsung Research upgraded the C-MIMO testbed to a D-MIMO one, with three RRHs connected from one CU by common public radio interface (CPRI) enabled fiber connection [29]. Each RRH has one antenna panel with four dual-polarized antenna elements, one field programmable gate array (FPGA) board with eight high-speed data converters, and RF circuits. For D-MIMO measurement results, this testbed shows a users-assisted OTA channel calibration method for seven user terminals at 3.5 GHz carrier frequency with 20 MHz LTE signal [29]. Another digital fronthaul D-MIMO testbed [30] is based on the open source OpenAirInterface platform from EURECOM [40]. This DRoF D-MIMO testbed has two remote RRHs, each with two antennas. The CU has Ethernet fronthaul links with the RRHs and supports commercial internet access. This digital D-MIMO testbed works on frequency division duplex (FDD) mode and DL/UL frequency is 2.66 GHz/2.54 GHz, respectively. In measurements, two commercial user terminals have Internet service from the testbed with six combinations of 5/10/20 MHz bandwidth signal, and two different fronthaul function splits. The systems conclude the occupied resources of different combinations [30].

A real-time SDM-enabled 2×2 D-MIMO system [31] works at 3.5 GHz carrier frequency with 163.84 MHz bandwidth and demonstrates indoor D-MIMO communication in seven cases to compare with SISO cases. This work has been extended to have UL direction with two RRHs, each of which has four antenna elements [17]. The antennas work in TDD mode so that UL and DL can share it by switching [17]. Another SDoF-based massive D-MIMO testbed has 12 distributed RRHs and works at 2.365 GHz carrier frequency with a single carrier 35 MHz 64-quadrature amplitude modulation (64-QAM) signal [16]. This massive D-MIMO testbed allows simple C-RAN structure by having offline signal processing and shows better communication signal quality than the C-MIMO case in an indoor measurement.

Paper [A] designs a user terminal with a robot car and makes the SDoF-based massive D-MIMO testbed an automatic testbed suitable for any MIMO measurements. The massive measurement results in Paper [A] can experimentally show the statistical capacity advantage of D-MIMO system over C-MIMO. Section 2.4 describes the detailed MIMO measurements and statistically analyzed results.

3.2 Communication Simulations

There are theoretical simulations available for MIMO capacity study.

3.2.1 MIMO Simulation Example

The simulation in [51] puts 100 RRHs for 40 users at 1.9 GHz carrier frequency with 20 MHz bandwidth and considers a model with channel estimation and power control abilities. With this close-to-reality configuration, [51] simulated user capacity for cell-free MIMO (D-MIMO) and small-cell MIMO (C-MIMO) at uncorrelated and correlated fading. The result in [51] concludes that D-MIMO improves user capacity fivefold in uncorrelated fading and tenfold in correlated fading over C-MIMO. Asymptotic analysis in [52] proves that D-MIMO gets more capacity gain

than C-MIMO when the system has a large number of antennas. The analytical and simulation results in [53] are from a specific high-speed train case with a MIMO system and conclude that D-MIMO offers more uniform user capacity than the C-MIMO. However, these simulations do not have an actual measurement reference to compare.

3.2.2   Raytracing MIMO Simulation

The work in [54] has an indoor MIMO simulation using a raytracing method based on geometrical optics. The simulated narrowband signal frequency is 2.45 GHz for four transmitters and 2500 receiving positions. This simulation model only considers line-of-sight propagation by having the maximum reflection number of three for six MIMO cases (three C-MIMO and three D-MIMO). The results plot a capacity map for all cases, and the D-MIMO has the more uniform capacity distribution for an IID fading channel.

   In a recent master's thesis project at the Microwave Electronics Laboratory (Department of Microtechnology and Nanoscience, Chalmers University of Technology) studies MIMO communication with raytracing-based electromagnetic propagation [55]. This master thesis work gets the MIMO channel response as a complex value by comparing the phase/amplitude information between the original and propagated signals. Subsection 3.3.4 presents the detailed MIMO simulation results, and subsection 3.3.5 compares the simulation with the measured results.

3.3   Comparison Between C-MIMO and D-MIMO in an Indoor Environment

The research results of [56] claim that D-MIMO can reduce the distance to users and offers larger capacity gain than traditional MIMO by equal-power allocation. The channel model in [56] considers path-loss, log-normal fading, and Rayleigh fading to the conclusion, proving that the receiver's location affects the MIMO capacity. This section statistically compares C-MIMO and D-MIMO in an indoor environment.

3.3.1   Environment Description

The automatic MIMO testbed in paper [A] has been used to perform C-MIMO and D-MIMO measurements in an indoor office area of 8 m × 10 m. The area is a rich multipath environment since the area covers an open office, a separate office, a kitchen, a meeting room, and laboratories. The C-MIMO and D-MIMO measurement layouts are in Figure 3.1a and Figure 3.1b, respectively. The only difference between the two measurements are locations of RRHs. The C-MIMO measurement puts all RRHs at one corner of the layout as in a conventional case. In comparison, the D-MIMO measurement equally distributes RRHs around the area. For both cases, the automatic receiver collects channel information and MIMO information following the positions marked as 1 − 44 one at a time.
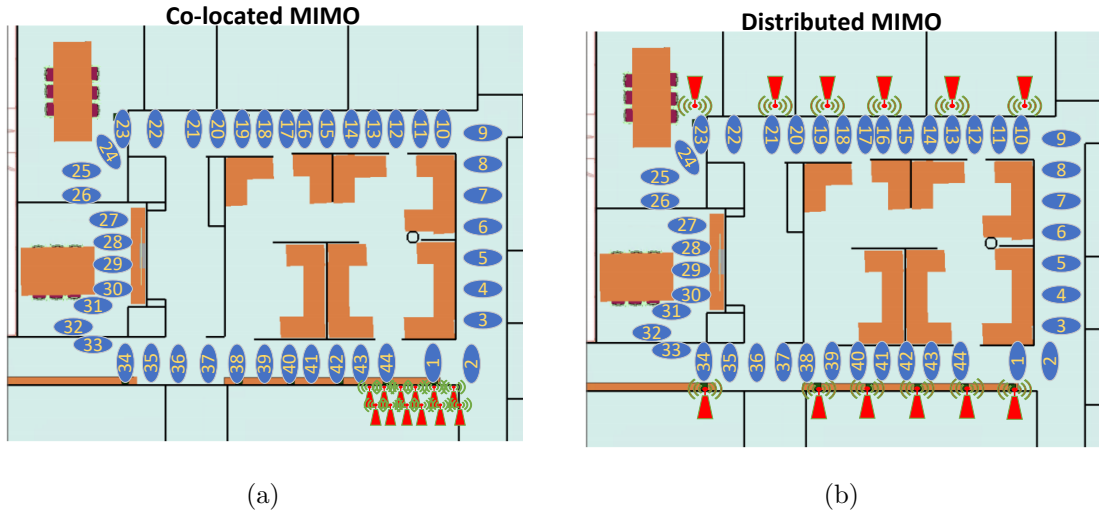
Figure 3.1: The MIMO antenna configuration with measured positions in the indoor 8 m × 10 m area. (a) C-MIMO; (b) D-MIMO.
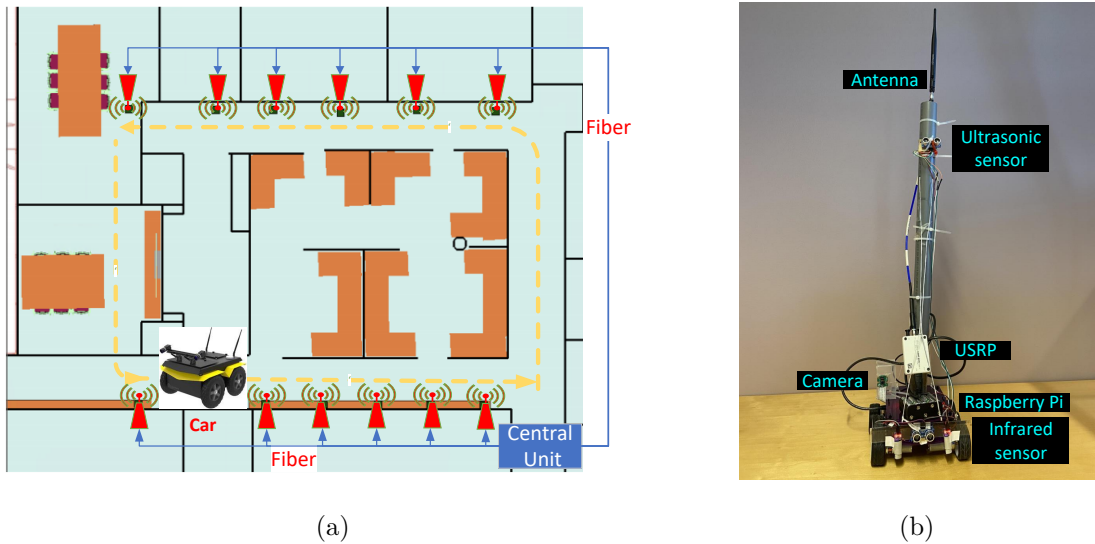
Figure 3.2: The automatic MIMO measurement setup in the indoor 8 m × 10 m area. (a) Indoor measurement area; (b) The designed automatic receiver.

3.3.2 Experimental Setup

The publication [16] shows an SDoF downlink testbed with 12 independent RRHs for MIMO measurements. Paper [A] extends this system with an automatic receiver to do extensive MIMO studies. Figure 3.2a shows an indoor area where distributed RRHs are located, and the automatic robot-based receiver can run freely. In Figure 3.2b, the automatic receiver is a robot car that carries a software-controlled RF receiver (USRP [57]) with an omnidirectional antenna. The automatic receiver also has an ultrasonic sensor, infrared sensors, and a camera to follow measurement positions labeled on the ground.

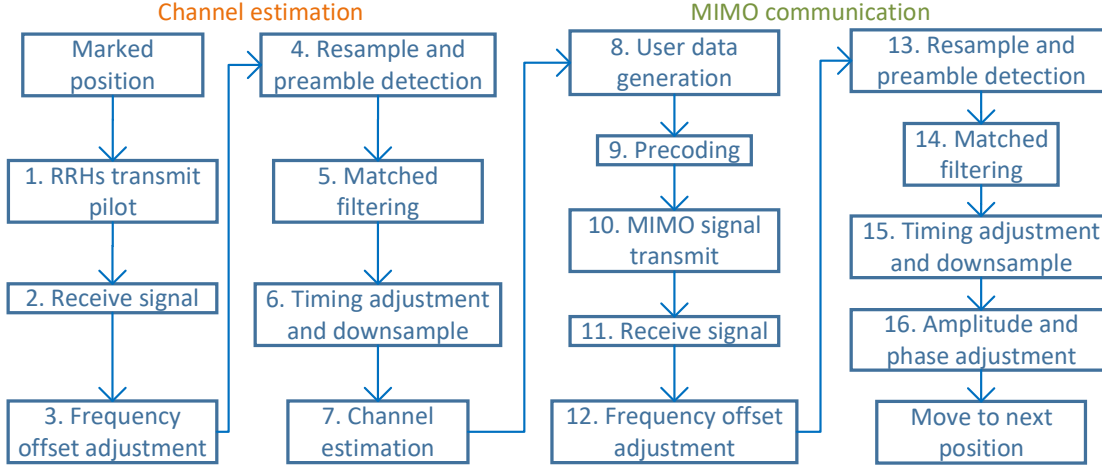Channel estimation   MIMO communication

Figure 3.3: The operation procedure of the automatic MIMO measurement testbed [A].

The automatic receiver processes several steps at each position, as Figure 3.3 shows. In the channel estimation procedure, the RRHs transmit the pilot signal in the first step, and the automatic receiver downconverts the received signal to the baseband in the second step. Steps 3 – 6 do frequency offset adjustment, resample with preamble detection, matched filtering, timing adjustment, and downsampling to the 7th step of least-square channel estimation. For the MIMO communication procedure, steps 8 – 10 generate user data with ZF precoding, as described in Section 2.3. The automatic receiver captures data again in the 11th step for RX baseband signal processing of steps 12 - 16. After these 16 steps, the automatic receiver finishes the measurements at the current position and moves to the next one.

3.3.3   Experimental Results

Figure 3.4 summarizes the received power and the normalized mean square error (NMSE) results for C-MIMO and D-MIMO measurements at 44 positions with 5 MHz bandwidth signal at 2.365 GHz center frequency. The NMSE results for C-MIMO and D-MIMO are solid orange and dashed orange curves, respectively. The NMSE curves fluctuate between -26 dB and -21 dB for both cases, which means that all positions have reasonable communication performance at any measurement. The received power for C-MIMO and D-MIMO are solid blue and dashed blue, respectively. The dashed blue curve is uniform around -50 dBm and shows that D-MIMO distributes power equally for users. In comparison, the solid blue of C-MIMO varies from -80 dBm to -35 dBm and drops dramatically for positions 23 – 35, which are not in the line-of-sight (see Figure 3.1).

From the collected channel matrix, the capacity expression of user m for MIMO cases is given by [58]

$$C_m = \log_2\left(1 + \sigma_m^2 \frac{S}{N}\right) [\text{bit/s/Hz}], \qquad (3.1)$$
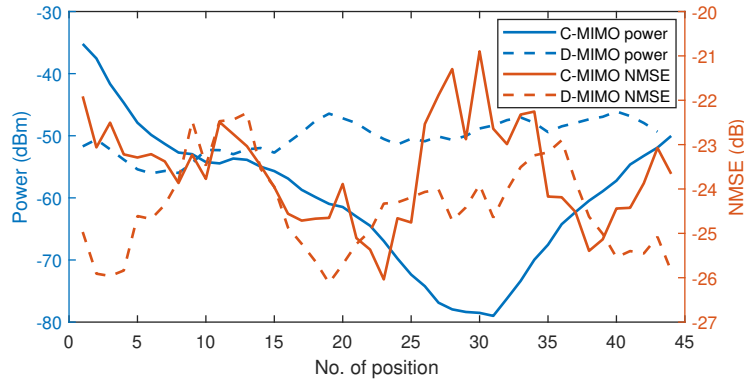
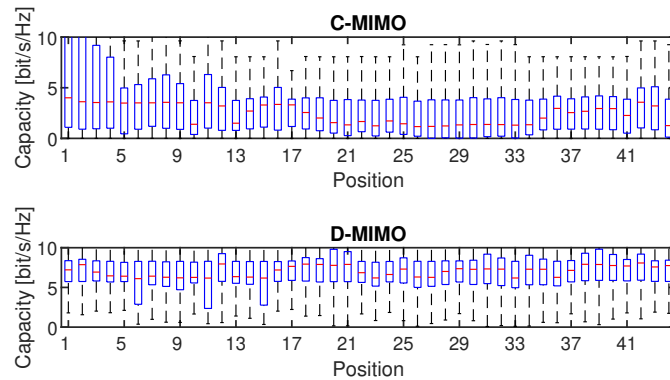Figure 3.4: The power and NMSE results of the MIMO measurements [A].

Figure 3.5: The boxplot of user capacity variation in MIMO measurements [A].

where C_m is capacity for user m and $\frac{S}{N}$ is SNR. σ_m^2 is the channel weight and is the mth eigenvalue obtained by singular value decomposition of the $12 \times M$ MIMO channel matrix.

An assumed scenario with 50000 randomized sets of 4 user locations among the 44 positions has been studied for statistical analysis. The corresponding user capacities have been determined from (3.1) using eigenvalues obtained from the decomposition of the measured channel matrices with with an assumption of 30 dB SNR. The user's capacity depends on combinations with the other three users. Figure 3.5 illustrates the user capacity distribution as a box-plot organized versus location. The capacity in C-MIMO shows a significant variation depending on the position of the other users, particularly for positions 1-4, which are close to the co-located RRHs. The locations, far away from C-MIMO antennas, have low capacity. On the other hand, D-MIMO can promise a stable and higher median capacity for all positions.

3.3.4 Simulation Results

The automatic testbed measurements of paper [A] are supported by the master's thesis report [55] using raytracing-based electromagnetic propagation in the simulation software [59]. The software needs a three dimensional (3D) measurement area model
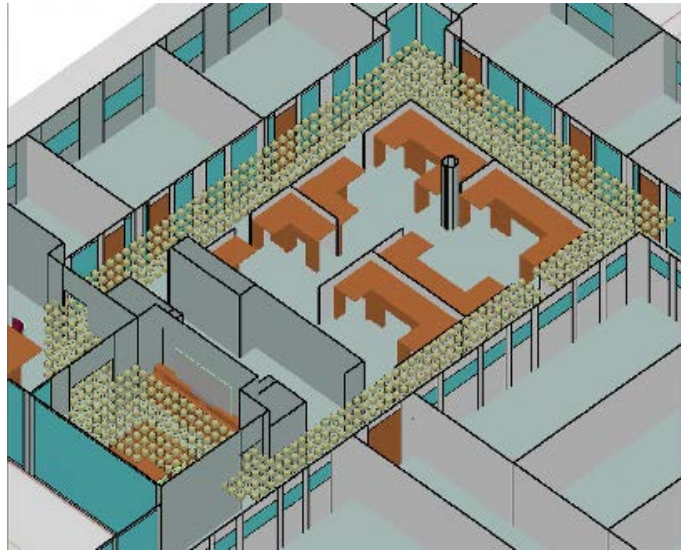
Figure 3.6: The 3D simulation model with 831 user positions for the indoor 8 m × 10 m area [55].
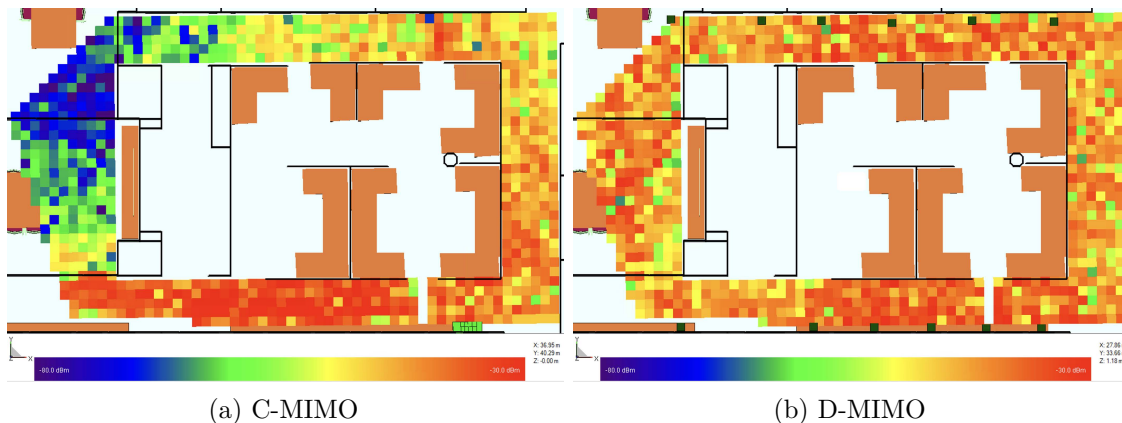
(a) C-MIMO

(b) D-MIMO

Figure 3.7: The heatmap of MIMO received power [55].

with material parameters of the walls, ceiling, floor, desks, and chairs. The 3D model with labeled positions is in Figure 3.6 and also includes RRHs as in real measurements. The simulation has 831 user locations and results in 12 × 831 C-MIMO and D-MIMO channel responses, in which 12 × 44 channel responses are for comparison with measurements.

The simulation software also gives a power distribution heatmap in Figure 3.7. At the C-MIMO heatmap, there is an apparent low power area in green and blue colors, and the high power area is concentrated around co-located RRHs in one corner. In comparison, the D-MIMO heatmap has a more uniform power distribution and does not show noticeable power variations.

The sum capacity is calculated for one 12 × 4 case based on (3.1). Reducing the number of RRHs helps power savings but affects channel capacity. In Figure 3.8, when removing one RRH, the C-MIMO user sum capacity is only 16 bit/s/Hz, and D-MIMO has a 20 bit/s/Hz user capacity. After 7 RRHs were removed, the
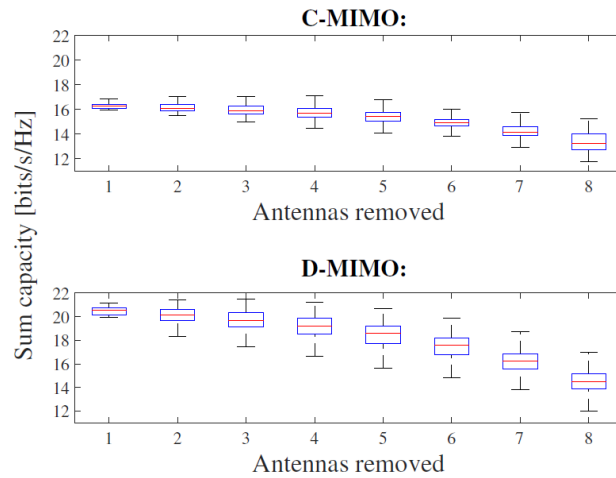
Figure 3.8: The MIMO capacity when reducing 1 - 8 RRHs [B].
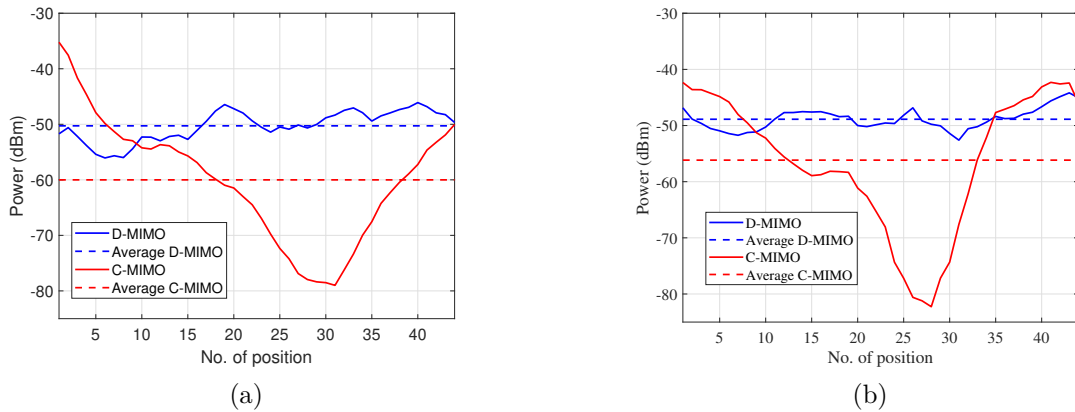
Figure 3.9: The received power during MIMO transmission in (a) measurement [A]; (b) simulation.

D-MIMO still shows the same user capacity as C-MIMO with one RRH removed. It proves that D-MIMO can give the same service as C-MIMO with fewer RRHs.

3.3.5 Measurement versus Simulation

Since the measurements and simulation are made for the same indoor environment, it is possible to do a direct comparison of received power and user capacity probability.

The MIMO received power of measurements, and simulation is shown in Figure 3.9a and Figure 3.9b. The blue curves are D-MIMO received power for measurements and simulation, and they agree with each other by fluctuating around -50 dBm. Both red curves show relatively limited received power at positions 23 - 35 at measurements and simulation. Hence, the MIMO received power indicates excellent agreement between measurements and simulation.

The 12×44 MIMO scenario with 4 randomly chosen user positions among the 44 measured locations has 135,751 unique 12×4 combinations. All user capacities
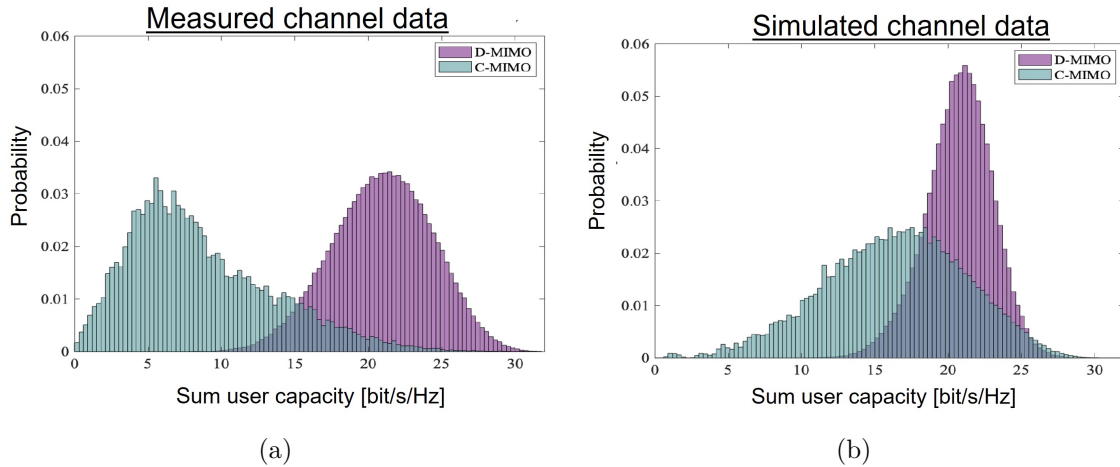
Figure 3.10: The MIMO channel capacity histogram in [B]. (a) measurement; (b) simulation.

of possible combinations are calculated using equation (3.1), and the probability is plotted in Figure 3.10a/Figure 3.10b for measurements and simulations. The D-MIMO generally has a higher user capacity of 22 bit/s/Hz than the C-MIMO, which has an average sum capacity of 7 bit/s/Hz (in measurement) and 16 bit/s/Hz (in simulation). Specifically, the C-MIMO's central user capacity differs between measurements and simulation. This difference comes from the uncertainties in material parameters and geometrical definitions. However, it does not affect the general results and conclusions.

3.4   Chapter Conclusion

This chapter has presented an automated radio testbed suitable for D-MIMO, C-MIMO, and other applications. Moreover, this chapter also studied the statistical analysis of channel capacity for the measurements of D-MIMO and C-MIMO in an indoor environment. The capacity predictions made with a raytracing-based electromagnetic propagation software show relatively good agreement with measurement data.

Chapter 4

mm-wave RoF MIMO Link

To serve more user devices/data subscriptions, RoF technology needs to work on larger bandwidth and, therefore higher data rate. The mm-wave signals can introduce more bandwidth for RoF than a lower-frequency band. Moreover, MIMO technology helps to overcome high path loss of mm-wave and increase capacity through spatial multiplexing. This chapter provides an overview of available mm-wave RoF architectures with examples and introduces an innovative mm-wave SDoF link architecture for MIMO applications. The proposed architecture is verified and demonstrated with conclusions.

4.1   mm-wave RoF Architectures

Section 2.5.2 introduces low-frequency RoF architectures which are not suitable for mm-wave frequency. In this section, several RoF architectures suitable for mm-wave operation are presented, starting with the ones already published in literatures.

4.1.1   Analog RoF

There are two mm-wave ARoF architectures in Figure 4.1. Both start with a digital IF signal because it is impractical to upconvert a baseband signal directly to mm-wave frequency. Having a digital IF signal at the beginning also helps to simplify hardware connections of an I/Q baseband signal and avoids the potential I/Q imbalance problem. The first architecture of Figure 4.1a transmits the analog IF signal from the CU to the RRH through a fiber connection. In the RRH, the mixer and the oscillator upconvert the IF signal to mm-wave frequency before feeding the PA and the antenna. The antenna could be a phased array antenna for an analog beamforming RoF system [60]. The second architecture of Figure 4.1b includes the mm-wave conversion in the CU after the analog IF signal from the DAC block. In this way, the fiber transmits the mm-wave signal to a simple RRH, which only has O/E and PA functions. Such a simple and phase coherent RRH enables massive MIMO applications for high-capacity RAN infrastructure. However, the modulation signal of the optical modulator/photodiode has limitations for higher frequency in the electrical/optical (E/O) and O/E functions. In conclusion, Figure 4.1a has a
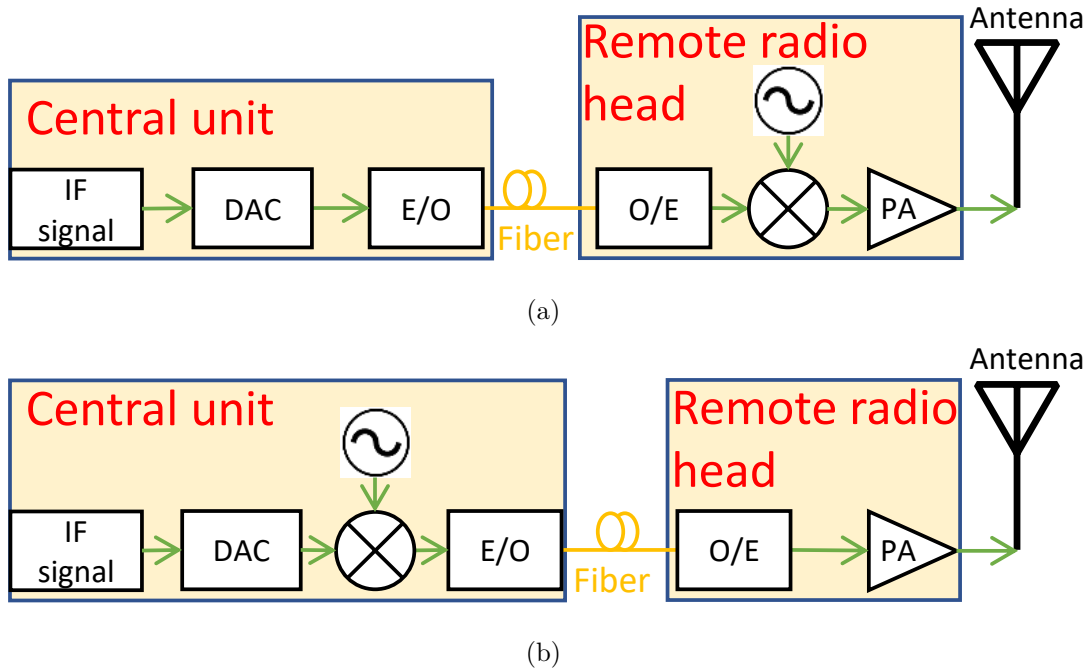
(a)

(b)

Figure 4.1: The mm-wave Analog-Radio-over-Fiber architecture illustrations. (a) The mm-wave signal generated in the remote radio unit; (b) The mm-wave signal generated in the central unit.

simple fiber connection with a complex RRH, while the second architecture of Figure 4.1b has a complex fiber connection with a simple RRH.

Several mm-wave ARoF SISO experiments have been implemented with laboratory equipment [60]–[62]. The work in [61] is compatible with the structure of Figure 4.1b and generates quaternary-amplitude-shift-keying (4-ASK) modulated 35.75 GHz at the CU. The study in [60] shares the optical oscillation signal from the CU and generates an optical mm-wave signal at 28 GHz in the RRH. The ARoF in [62] transmits an mm-wave signal from the CU and applies a photodetector in the RRH to recover the electrical mm-wave signal. An ARoF-enabled 2×1 MISO demonstration [63] works on 28.4 GHz carrier frequency with an outphasing principle. However, they are far from working as real solutions with commercial components and have limitations for coherent MIMO extension.

There are several mm-wave ARoF-based D-MIMO solutions. The results, in [64], reached the highest data rate of 328 Gbit/s with 2×2 MIMO antenna configurations. However, this system works as two independent SISO systems based on narrow beam horn antennas and can not support MIMO precoding [64]. The study in [65] transmits analog IF signals and synchronization clocks to RRHs. The demonstration results have 800 MHz bandwidth at 28 GHz frequency [65]. However, the ARoF architecture suffers from optical signal distortion [32] [33].

4.1.2 Optical Beamforming

Another interesting mm-wave RoF study is the optical beamforming topic based on ARoF structure. Figure 4.2 summarizes the available mm-wave optical beamforming RoF structures, which all generate mm-wave RF signals in the CU. The systems in [66], [67] are based on the illustration in Figure 4.2a, where the CU feeds the optical modulated RF signal from E/O into several branches with different time delay δ_n. The fiber connection is a multi core fiber (MCF) which transmits optical signals, each with different with time delay δ_n. In the RRH, each branch of the optical signals has an individual O/E to recover RF signals with optical time delay δ_n for the following phased array antenna. The time delay of the optical signal corresponds to the phase delay of electrical RF signals at the input of the phased array antenna. In the demonstration of [66], optical delay lines and attenuators change the amplitude/phase of the seven optical signals to have the optical beamforming function at 60 GHz for 1.76 GHz bandwidth. The research in [67] employs optical ring resonators for the optical signal time delay in CU to have mm-wave beamforming functionality. The CU thermo-optically adjusts the heaters to have different time delays for the optical beamforming, and the system successfully demonstrates 3 GHz bandwidth for a 19 GHz RF signal.

In the second mm-wave optical beamforming RoF structure, the fiber connection can be a single mode fiber between the CU and the RRH as Figure 4.2b. The RRH divides the received RF optical signal N times and assigns the time delay δ_n for each branch, followed by O/E and phased array antenna. The system in [68] designs a switchable optical time delay circuit in the RRH and reports the mm-wave optical beamforming with 2.2 GHz bandwidth (13.2 Gbit/s data rate) at 28 GHz carrier frequency. The final mm-wave optical beamforming RoF structure is proposed in the study [69] as Figure 4.2c. The system in [69] can configure nine wavelengths for the optical modulator in the CU. In the RRH, each optical signal wavelength is converted to the electrical domain by the individual O/E converter. The array antenna has nine individual input ports, which decide nine different beamforming fixed directions. A 64-QAM OFDM signal with 100 MHz bandwidth is used for OTA measurements at 28.25 GHz carrier frequency [69].

All three structures of Figure 4.2 need a Mach-Zehnder modulator (MZM) and external laser to modulate RF signal to the optical domain and have the same system complexity. However, there is main difference comes from the fiber link. Because MCF is mostly suitable for a short distance of connection due to modal dispersion, while single mode fiber (SMF) solution needs a precise laser-fiber interface and can work for several tens of kilometers distance.

4.1.3 Digital RoF

Figure 4.3 illustrates the digital RoF architectures proposed for mm-wave systems. The first architecture in Figure 4.3a is based on the low-frequency structure and includes an upconversion function to generate an mm-wave signal in the RRH. The fiber link transmits CPRI or Enhanced CPRI (eCPRI) data between the CU and the RRH. The DSP supports the fiber data protocols and feeds the high-speed DAC.
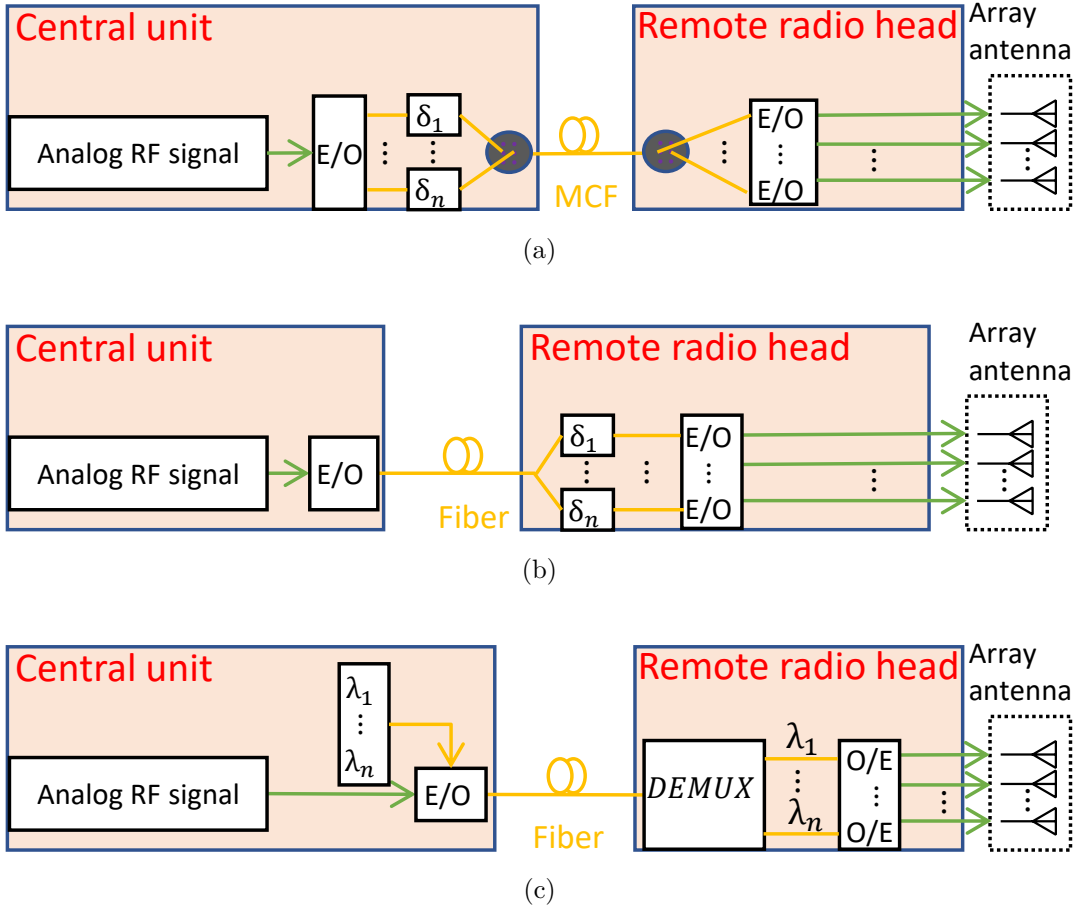
Figure 4.2: The mm-wave optical beamforming Radio-over-Fiber architecture illustrations. (a) Hardware delay in the cental unit enabled optical beamforming architecture; Multi core fiber (MCF); (b) Hardware delay in the remote radio head enabled optical beamforming architecture; (c) Multiple wavelengths enabled Optical beamforming architecture; Demultiplexer (DEMUX).

Similar to the architecture in Figure 4.3b, a SDoF system was proposed in [70]. The work in [70] uses a bandpass filter to suppress the out-of-band SDM quantization noise. It enables distributed MIMO operation with coherent LO signals from the clock data recovery (CDR) and the phase-locked loop (PLL). A 160.32 MHz bandwidth is presented for a 2×1 MISO configuration. However, this bandwidth is limited by the 10 Gbps data rate of the fiber connection and phase noise of the phase-locked loop (PLL) used [70]. Then, an SDoF solution with real-time SDM is studied, with a 100 Gbps bitrate, for the demonstration of 22.75 GHz – 27.5 GHz carrier frequency range achieving symbol rate of 390 Msym/s performance [71].

4.2   mm-wave SDoF MIMO Link Architecture

The SDM digital RoF architecture with the system above has phase noise and a limited symbol rate. Hence, this section proposes IF SDoF and baseband SDoF
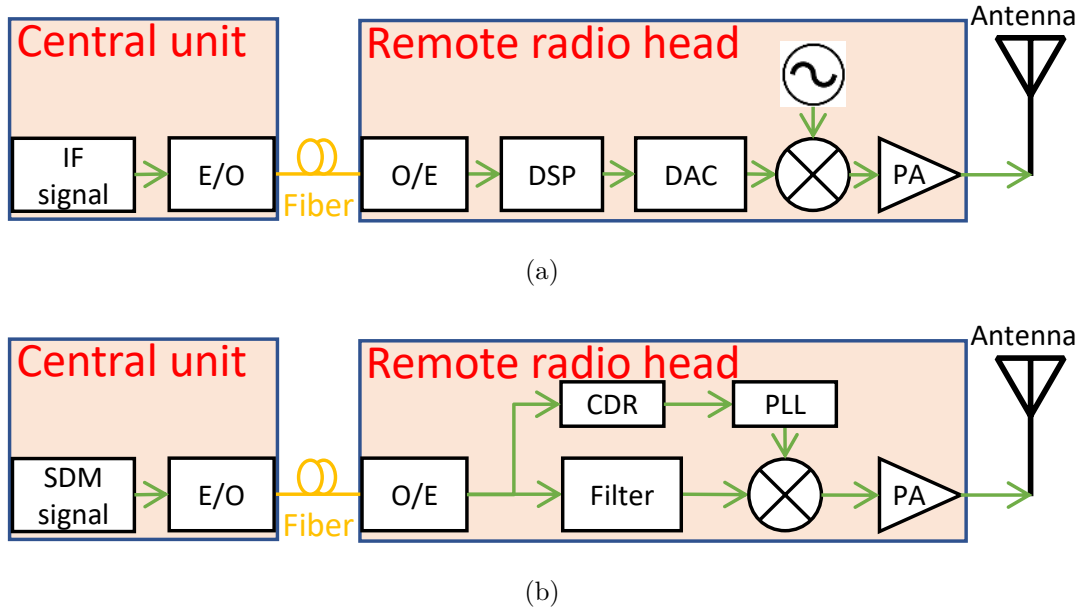
Figure 4.3: The mm-wave Digital Radio-over-Fiber architecture illustrations. (a) CPRI or eCPRI based; (b) Signal-delta modulation based.

MIMO link architectures. Below, these proposed architectures are studied in more detail.

4.2.1 IF SDoF

Paper [C] proposed an innovative mm-wave IF SDoF MIMO link architecture based on a quad small form-factor pluggable 28 (QSFP28) fiber connection as illustrated in Figure 4.4. The QSFP28 is a standardized and commercially available module, which has four independent subchannels at 25 Gbps data rate. The architecture is based on using SDM coded IF with remote LO for upconversion. The CU generates four parallel and coherent bandpass sigma-delta modulation (BPSDM) bit streams offline from four IF digital signals. The FPGA board connects with the personal computer (PC) and transmits four electrical bit streams to the QSFP28 fiber connection. The RRH consists of a QSFP28 transceiver, 90° hybrids, upconverters, and oscillation signals. The 90° hybrids connect with the outputs of QSFP28 to have quadrature IF signals for the single sideband upconverters. In theory, the SDM signals require a bandpass filter to recover analog IF signal [72]. However, the 90° hybrids and the inputs of upconverters can act as bandpass filters in this implementation. The RRH feeds four independent inputs of an array antenna. This way, the CU can digitally, remotely, and fully control the independent four-channel signals for this mm-Mave MIMO link architecture.
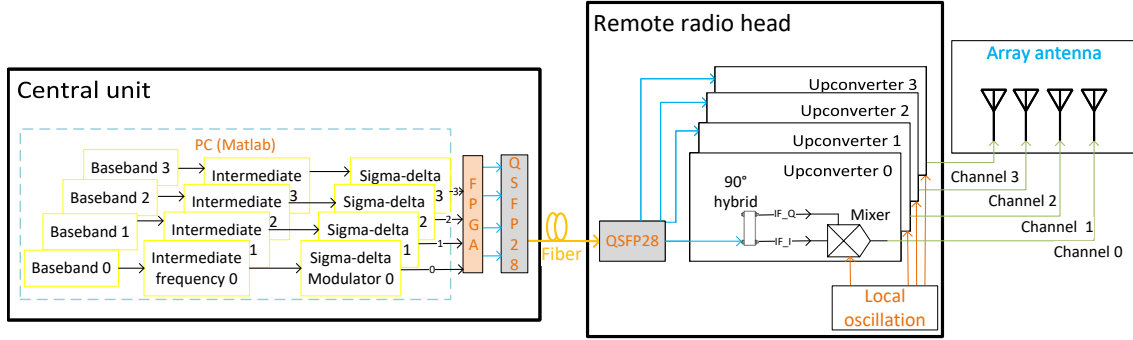
Figure 4.4: The proposed mm-wave IF SDoF architecture [D].
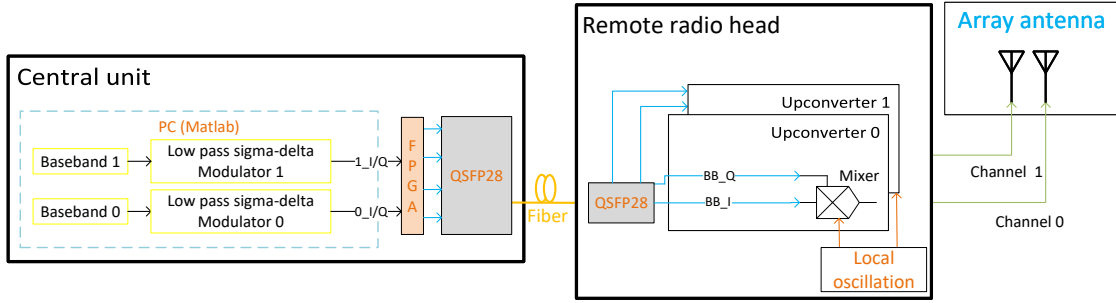
Figure 4.5: The proposed mm-wave baseband SDoF architecture.

4.2.2   Baseband SDoF

The QSFP28 fiber connection-based architecture can also work with a baseband SDM principle as shown in an mm-wave baseband SDoF MIMO link architecture of Figure 4.5. The parallel low pass SDM modulates the I/Q branch of the baseband signal to a pair of bitstreams. The QSFP28 fiber connection transmits four bitstreams (two baseband SDM signals) to the RRH. The remote local oscillation and the mixer upconverts the baseband SDM bitstreams to an mm-wave signal which connects with the inputs of an array antenna.

4.2.3   Comparison

Figure 4.6 is the theoretical simulated NMSE results of the proposed mm-wave IF SDoF and baseband SDoF link for a single carrier 64-QAM signal at 25 Gbps. The blue curve is the IF SDM for the mm-wave IF SDoF link and has -23.3 dB NMSE at 1200 Msym/s. At the same time, the baseband SDM NMSE is still -38.9 dB NMSE at 1200 Msym/s. However, the baseband SDoF architecture can only support two baseband signals from each QSFP28 fiber connection, while the IF SDoF architecture transmits four IF signals. The IF SDoF architecture needs hybrids to do single sideband upconversion, while the baseband SDoF does not need it. The carrier frequency is more flexible for the IF SDoF architecture by changing the IF or LO frequency. On the other hand, only the LO frequency decides the carrier frequency

Figure 4.6: The IF SDM and Baseband SDM simulation results for IF SDoF and Baseband SDoF architectures.
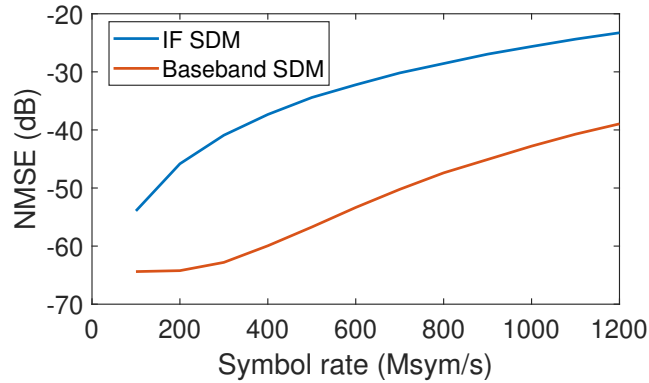
in the baseband SDoF architecture.

4.3 mm-wave SDoF MIMO Link Demonstrator

The previously proposed mm-wave IF SDoF structure is implemented with off-the-shelf components and verified in this section.

4.3.1 IF SDoF MIMO Link Implementation

The proposed architecture has been implemented for validation in paper [D], as in Figure 4.7. In the CU, the IF frequency is 2.2 GHz, the center frequency of the selected 90° hybrid. The oscillation frequency from the signal synthesizer is 6.45 GHz, with a built-in LO quadrupler in the mixer so that the RF frequency can be 28 GHz as 6.45 GHz $\times$ 4 + 2.2 GHz = 28 GHz. This architecture can radiate RF frequency up to 44 GHz by changing either the oscillation frequency or IF frequency. The mm-wave signals from the RRH feed to the linear array antenna with four independent inputs.

Paper [D] studies the power levels at different positions in the transmitter implementation. The positions labeled A/B/C in Fig. 4.7 have the average bandpower of -11.6 dBm/-15.7 dBm/-0.5 dBm, respectively. Position A's power is the same for all the QSFP28 output channels. At position B, the bandpower has dropped due to the loss of the 90° hybrid, SMA connector, and coaxial cable. The active mixer has a 15.2 dB gain for the mm-wave signal at position C.

At the receiver side, Vivaldi antennas are used and connected with a low noise amplifier (LNA) and a powerful Keysight VSA (N9042B UXA X-Series Signal Analyzer [73]). The VSA can verify the spectrum power levels and does down conversion for RX signal processing.

4.3.2   Hardware

All off-the-shelf hardware used for the TX implementation is reported in Table 4.1. The 90° hybrid (ZX10Q-2-27-S+) supports frequency from 1.7 GHz to 2.7 GHz. Therefore, the system bandwidth is limited to 800 MHz during the following measurement results. The power dividers (ZX10R-14-S+) can work up to 10 GHz and divide the LO signal into four upconverters. The upconverting mixers (EVAL-ADMV1013) are upconverters and generate frequencies up to 44 GHz in IF or baseband input signal mode.

Table 4.1: Commercial hardware list of the IF SDoF transmitter demonstrator.

Hardware	Manufacturer	Model	Quantity	Ref.
FPGA board	Xilinx	VCU128	1	[74]
QSFP28	FS	QSFP28-SR4-100G	2	[75]
90° Hybrid	Mini-Circuits	ZX10Q-2-27-S+	4	[76]
Power divider	Mini-Circuits	ZX10R-14-S+	3	[77]
Mixer	Analog Devices	EVAL-ADMV1013	4	[78]

Some technical specifications of the QSFP28 module used for the fiber connection are reported in Table 4.2. The connection between CU QSFP28 and RRH QSFP28 is made through a 10 m long cable with multifiber termination push-on (MTO-12) connectors at both ends. The cable includes twelve fibers, four of which transmit four data streams in this implementation. The maximum data rate can be 4×25.78 Gbps, and this implementation works on 4×25 Gbps.

Table 4.2: Technical specifications of the QSFP28 module used.

Specification	Description	Specification	Description
Wavelength	850 nm	Connector	MTO[a]-12
Media	Multi-mode fiber	Max fiber length	100 m
TX Type	VCSEL[b]	Receiver Type	PIN[c]
TX Power	-8.4 to 2.4 dBm	Max Data Rate	4x25.78 Gbps

[a] Multifiber Termination Push-on/Pull-off.
[b] Vertical Cavity Surface Emitting Laser.
[c] P-doped - Intrinsic - N-doped.

The TX antenna array has ports fed with the four parallel coherent signals from the RRH. The TX antenna is designed for 28 GHz frequency in CST Microwave Studio. The antenna consists of 16 patch elements in total, where each column has four fixed patch elements, creating a narrow elevation beam width. The half-power beamwidth of the TX antenna is 79.8°/20° in azimuth/elevation direction, respectively. The TX antenna is a linear array patch antenna and can steer the transmitted beam in the azimuth direction by controlling the phase of the inputs. The separation distance between elements in the azimuth/elevation direction is 5.35 mm/5.63 mm, respectively, corresponding to approximately a half wavelength at the center frequency.

4.3.3 Signal Processing

During the following OTA measurements, we are accounting for the total phase differences of the system by channel estimation and compensating for the phase differences by precoding. The MIMO link works in TDD mode in paper [C] and paper [D].

There are two steps for MISO or MIMO demonstration, and channel estimation is the first step. The orthogonal pilot signal $\mathbf{X}_\mathrm{p}$ is

$$\mathbf{X}_\mathrm{p} = \begin{bmatrix} \mathbf{x}_0 & \mathbf{0} & \mathbf{0} & \mathbf{0} \\ \mathbf{0} & \mathbf{x}_1 & \mathbf{0} & \mathbf{0} \\ \mathbf{0} & \mathbf{0} & \mathbf{x}_2 & \mathbf{0} \\ \mathbf{0} & \mathbf{0} & \mathbf{0} & \mathbf{x}_3 \end{bmatrix}_{N \times 4}, \tag{4.1}$$

where the $\mathbf{x}_0$, $\mathbf{x}_1$, $\mathbf{x}_2$, $\mathbf{x}_3$ and $\mathbf{0}$ have $N/4$ samples. Moreover, the least-square algorithm calculates the channel information $\widehat{\mathbf{H}}$ according to equation (2.16). The second step is the ZF MIMO precoding of user data, as explained in subsection 2.3.3. The MISO digital beamforming follows the precoding of subsection 2.2.2.

4.4 Wireless Communication Experiments

In this section, the implemented mm-wave IF SDoF MIMO link of the previous section is used to demonstrate wireless communication of digital beamforming MISO and MIMO experiments.

4.4.1 Prerequisites

Paper [D] studies the proposed IF SDoF architecture for MIMO applications extensively. The link characterization works on the setup of Figure 4.8 at a center frequency of 28 GHz.

All of the link characterizations are performed with a single-carrier 64-QAM signal. The mm-wave full-band output spectrum is shown in Figure 4.9a. As shown in the figure, the inband signal is at least 20 dB higher than the quantization noise, lower band image transmission, and LO leakage. The output signal has an adjacent channel power ratio (ACPR) of 30.6 dBc for a 100 MHz bandwidth signal as shown in Figure 4.9b.

Due to the hybrid's bandwidth, the symbol rate verification is limited to a maximum of 800 Msym/s in Figure 4.10. The bottom curve (Sim) in Figure 4.10 is the simulated SDM signal performance as a reference for measured results. Positions A/B/C are as labeled in Figure 4.7. Position B's performance is worse than position A's because of the power difference. The limitation of position C's performance is from the upconverter's noise figure and the noise floor of the VSA. The simulated result (Sim) is still 5 dB better than measurements at 800 Msym/s, which is reasonable for hardware performance, as the same results concluded in [16]. Generally, the measured results follow the simulated trend.
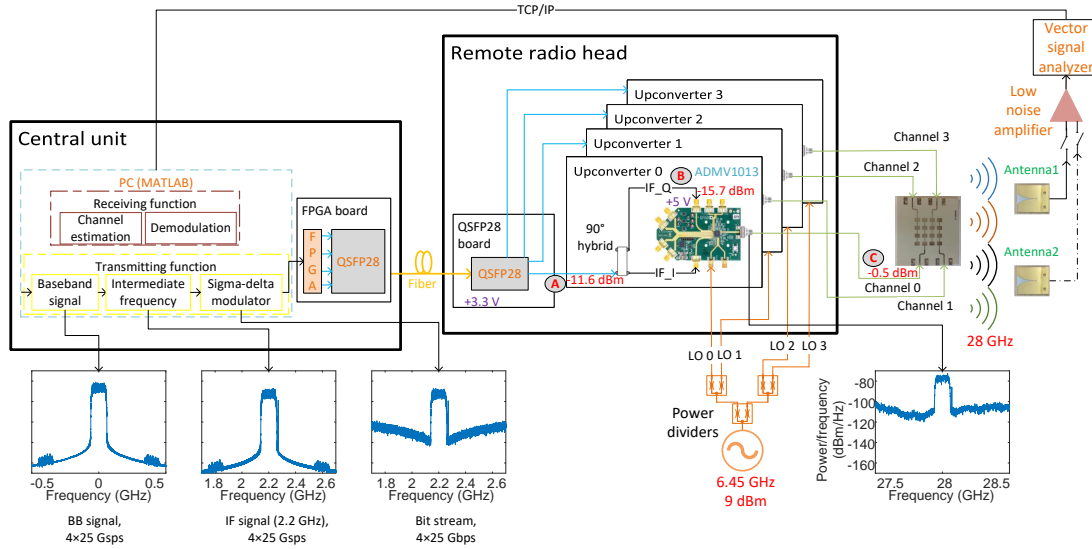
Figure 4.7: The link implementation with spectrum and power levels [D].
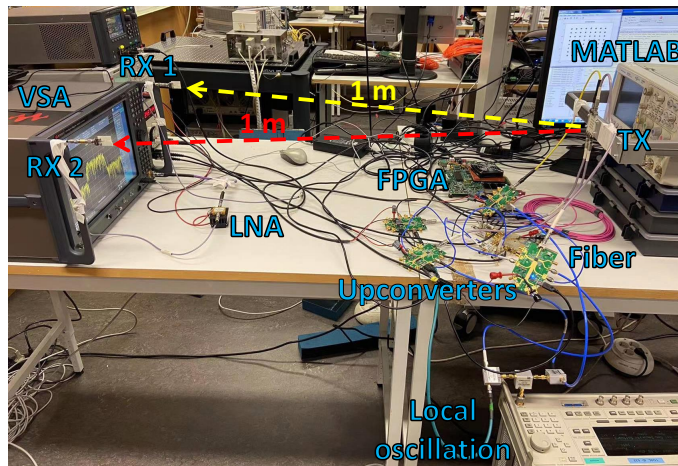

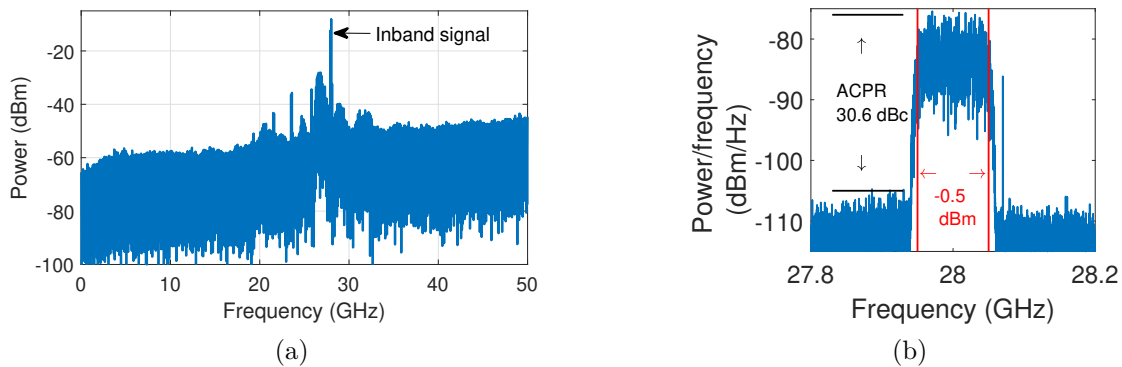Figure 4.8: The setup photo for link implementation [D].

Figure 4.9: The results of the link characterization with 100 MHz single-carrier 64-QAM signal [D]. (a) Output spectrum; (b) Adjacent channel power ratio (ACPR) and output bandpower.
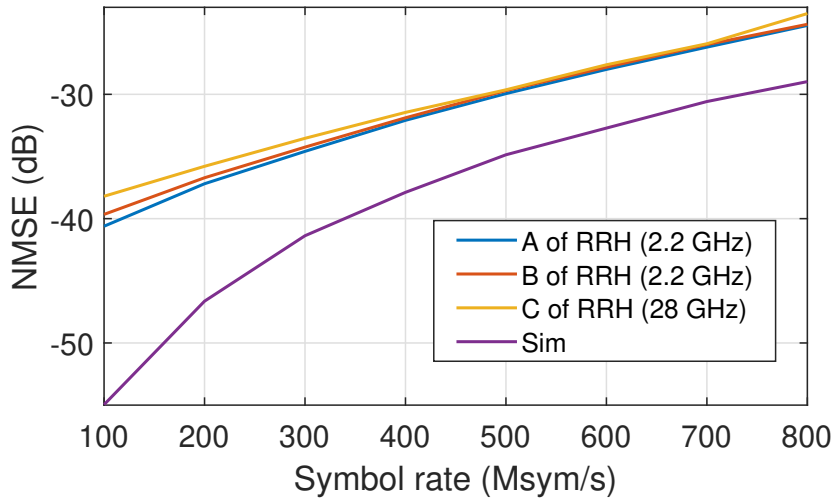
Figure 4.10: The results of the link performance characterization [D].

(a)   (b)
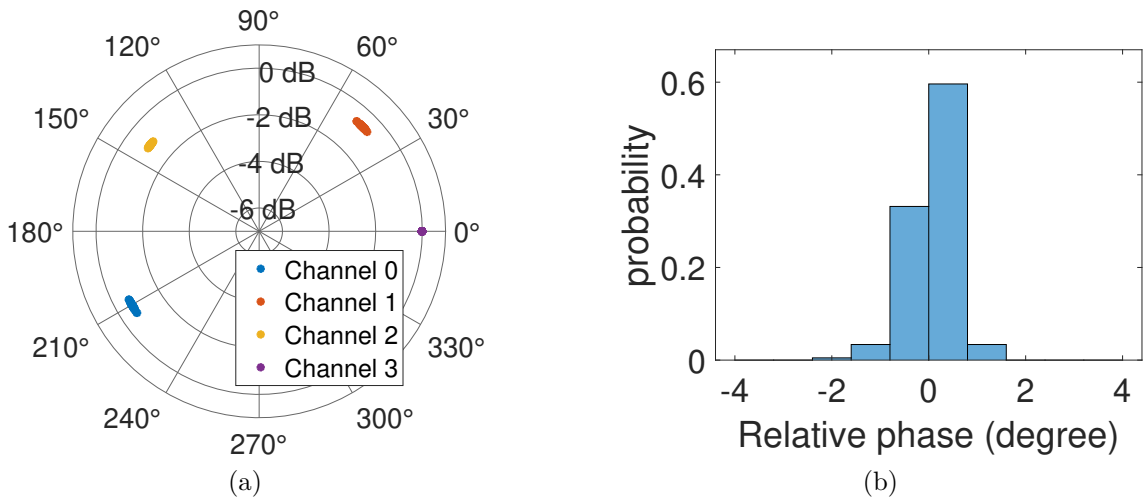
Figure 4.11: Channel information obtained in digital beamforming demonstration [D]. (a) Polar plot; (b) Normalized relative phase variations.

4.4.2   Beamforming MISO

The OTA demonstration includes SISO, MISO, and MIMO cases across a 1 m distance between RX and TX antennas. Moreover, those demonstrations will be introduced in the following subsections.

As introduced in Section 3.3, the digital beamforming demonstration needs two steps which are channel estimation and MISO beamforming. The TX radiates pilot signals at the channel estimation step, and the RX calculates the channel information. The 208 times repeated channel measurement results of the RX antenna 1 are presented in Figure 4.11a. The phase and amplitude of Channel 0/1/2 are normalized against Channel 3. The normalized {amplitude, phase} channel information is $\{-0.69\,\text{dB}, -150°\} / \{-0.69\,\text{dB}, 45°\} / \{-1.04\,\text{dB}, 142°\}$ for the channels Channel 0/Channel 1/Channel 2, respectively. Because the four elements of the TX antenna are mounted at the same height as RX antenna 1, the amplitude difference

(a)

(b)

(c)

(d)
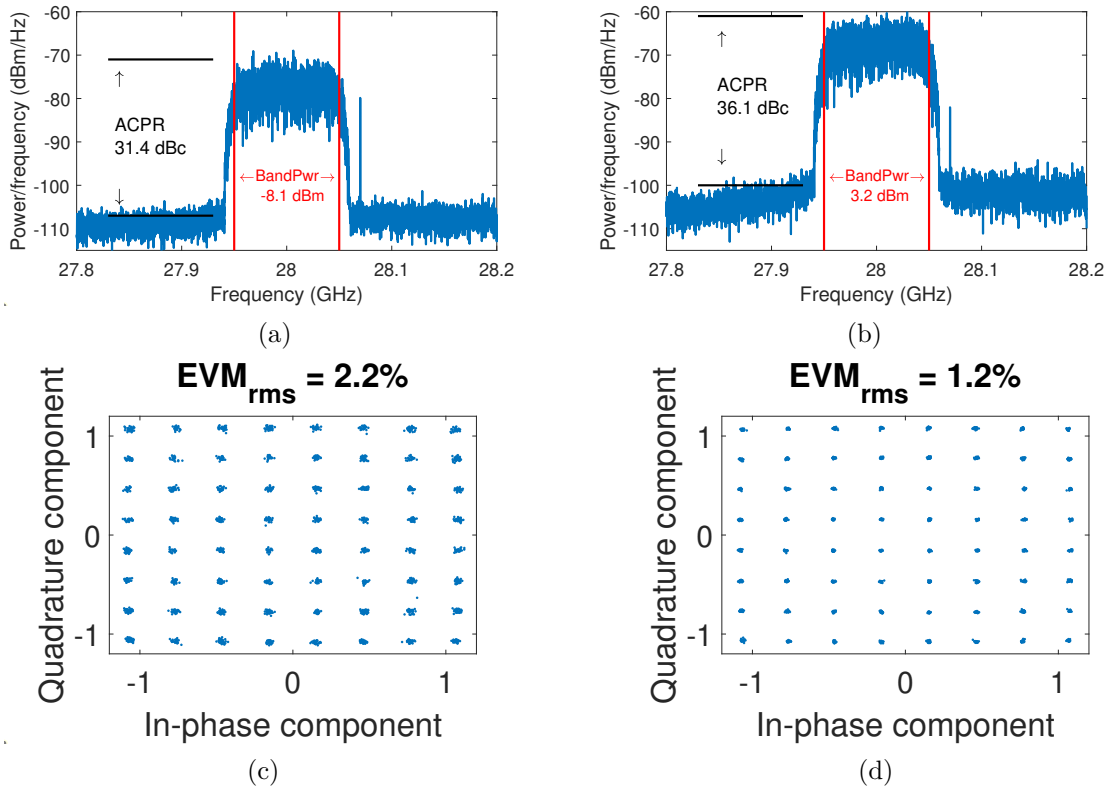
Figure 4.12: The received OTA performance in [D] of (a) SISO OTA; (b) MISO OTA; (c) SISO constellation; (d) MISO constellation.
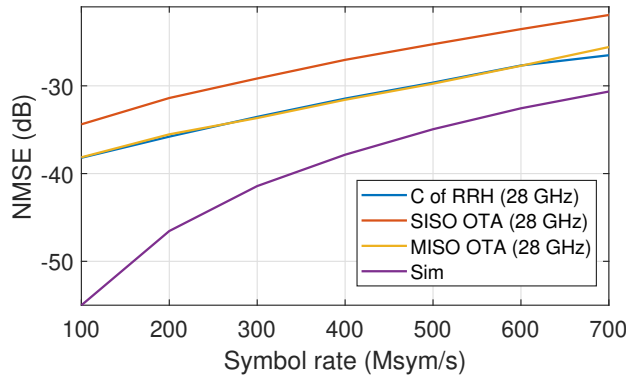
Figure 4.13: Performance of digital beamforming demonstration [D].

between the four channels is only around 1 dB. Figure 4.11b shows the histogram for the normalized phase variations of all channel coefficients with a maximum phase variation within -2° to 2° . This concludes that this MISO demonstration has stable and precise channel information.

In Figure 4.12, the MISO OTA received bandpower is 3.2 dBm and the SISO OTA case only has -8.1 dBm received bandpower. This means that the digital beamforming gives 11.3 dB more bandpower, and it is well matching with the theory which would suggest 12 dB beamforming gain for 4 antennas.
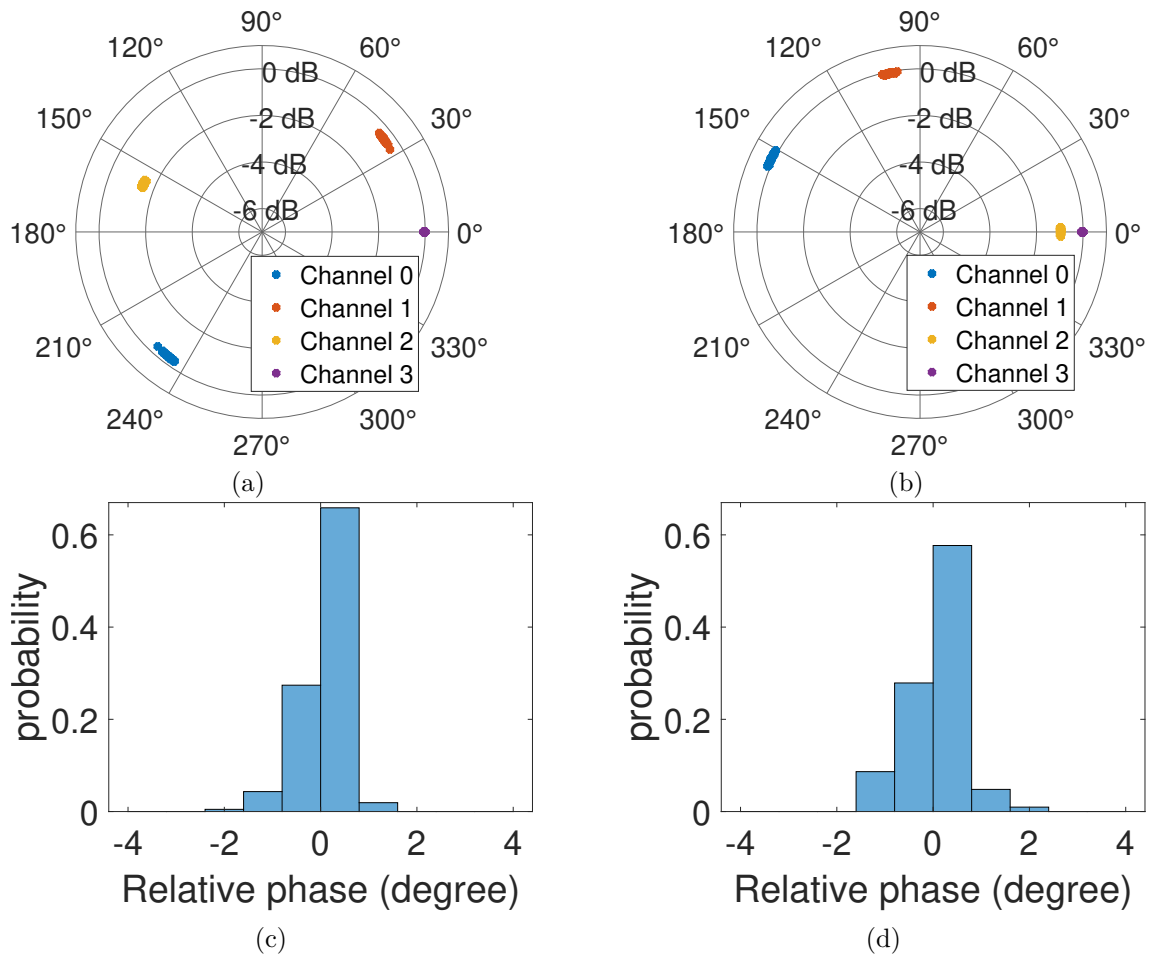
Figure 4.14: The channel estimation results from 225 repeated MU-MIMO over-the-air measurements [D]. (a) Polar plot of channel information for between transmitter and receiver with antenna1. (b) Polar plot of channel information for between transmitter and receiver with antenna2. (c) Histogram of normalized channel phase variations for antenna1. (d) Histogram of normalized channel phase variations for antenna2.

There are cable-connected mm-wave, SISO OTA, MISO OTA, and simulated NMSE results for up to 700 Msym/s symbol rate reported in Figure 4.13. The worst one is SISO OTA at the top and is limited by the high path loss of 28 GHz signal for a 1 m distance. When all TX sub-channels are active, the digital beamforming improves the NMSE to -25.2 dB, close to the NMSE at the upconverter output port (position C in Figure 4.7).

This proposed architecture demonstrated a digital beamforming function that improves the received power and NMSE performance with precise channel information.

4.4.3   MU-MIMO

The next demonstration is to evaluate the proposed architecture for a realistic MU-MIMO scenario. There are also two steps in the MU-MIMO communication demonstration: channel estimation and ZF MIMO communication. Since the system
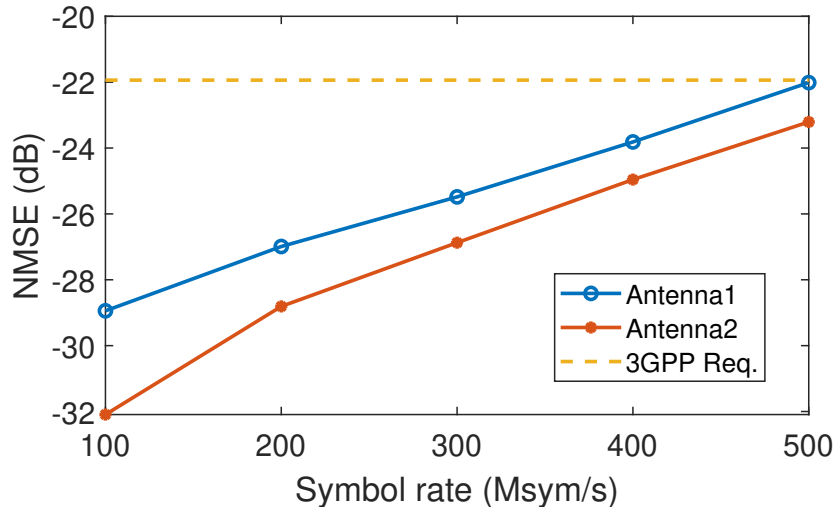
Figure 4.15: The symbol rate performance of MIMO demonstration [D].

only has one low noise amplifier LNA and one VSA, channel information must be collected one by one by switching cables between antenna 1 and 2. During measurements, antenna 1's channel information is collected first when TX radiates the pilot signal. The antenna 1's channel information is presented in Figure 4.14a and Figure 4.14c at a symbol rate of 100 Msym/s. The antenna 2's channel information is collected in Figure 4.14b and Figure 4.14d with 100 Msym/s. The normalized polar plots of two antennas are stable for 225 times repeated measurements, and the normalized relative phase variation is only -2° to 2° . This phase variation is the same as digital beamforming's result, which means the system works stable. Two RX antennas have different polar plots because they work independently.

The system can demonstrate MIMO communication for two independent users with stable channel information. Since antenna 2 connects with LNA from the previous channel estimation step, antenna 2 does MIMO communication before switching cable to antenna 1. During the experiments, the symbol rate was varied from 100 Msym/s to 500 Msym/s by repeating the channel estimation and ZF MIMO communication steps. Figure 4.15 shows the NMSE results of two users along with the 3rd generation partnership (3GPP) requirements. At 500 Msym/s, both users still have -22.1 dB and -23.3 dB NMSE, which satisfies the 3GPP requirements of 64-QAM modulation [79]. Antenna 2 is always better than antenna 1 based on NMSE results. Even if the demonstration changes the cable switching order, the results do not change. It shows that cable switching does not affect MIMO demonstration. Another limitation might be the position and radiation of RX/TX antennas causing a difference in the effective signal power received [80].

4.5 Chapter Conclusion

This chapter first introduces an innovative, flexible mm-wave SDoF architecture, and by demonstrations, it is then confirmed that this architecture is a feasible and

close-to-reality solution. The step-by-step power study and bandwidth verification validate system performance by measurements.

Table 4.3 compares this demonstration with the state-of-the-art RoF publications. There are ARoF and SDoF architectures for the mm-wave band. From the table, it is concluded that this demonstration has the highest symbol rate for SDoF publications. This architecture can also be a building block for a D-MIMO system in the future.

Table 4.3: Comparison with state-of-the-art RoF publications.

Ref.	RoF	MIMO	Symbol rate	OTA	Carrier	NMSE
[60]	ARoF	1×1	1.96 Gsym/s	2.2 m	28 GHz	-14 dB[a]
[81]	ARoF	2×2	1 Gsym/s	10 m	28 GHz	-24.3 dB
[69]	ARoF	9×1	100 Msym/s	6.3 m	28 GHz	-31.3 dB
[64]	ARoF	2×2[b]	22 Gsym/s	0.2 m	140 GHz	-14 dB[a]
[82]	ARoF	2×1	3 Gsym/s	1.5 m	28 GHz	-23 dB
[66]	ARoF	8×1	3.5 Gsym/s	0.5 m	60 GHz	-19.6 dB
[70]	SDoF	2×1	160.32 Msym/s	2.0 m	> 24 GHz	-24.4 dB
Paper [D]	SDoF	4×1	700 Msym/s	1.0 m	28 GHz	-25.2 dB
Paper [D]	SDoF	4×2	500 Msym/s	1.0 m	28 GHz	-22 dB

[a] The paper repoets the bit error rate (BER) corresponding to forward error correction (FEC) with 25% overhead. The NMSE requirement for this BER is -14 dB [83].

[b] This is only antenna configuration and does not have MIMO precoding.

Chapter 5

Conclusions and Future Work

5.1 Conclusions

This thesis studied fiber-connected wireless MIMO communication systems to increase channel capacity for future beyond-5G and 6G systems. The MIMO capacity is statistically investigated with an automatic measurement testbed and a raytracing-based electromagnetic propagation software. We also proposed an innovative wideband mm-wave SDoF link architecture for future mm-wave D-MIMO systems.

A MIMO testbed is designed with 12 RRHs and one automatic receiver to study MIMO capacity. The automatic receiver is a radio frequency receiver mounted on a programmed robot car that can go anywhere as a user. Using this testbed, the automatic testbed collected 44 users' channel information in an indoor environment with D-MIMO and C-MIMO antenna configurations. Furthermore, a raytracing-based electromagnetic propagation software did a channel simulation for the same indoor area. The thesis calculates MIMO capacity by deriving traditional Shannon capacity. By calculating MIMO capacity with randomly selected four-channel information, the probability results show that the D-MIMO channel has a higher capacity than the C-MIMO case. The box plot results prove that the D-MIMO gives more uniform capacity for any random combinations than C-MIMO.

The mm-wave band has wider bandwidth than a low-frequency signal and can support more high-capacity applications. But mm-wave signal has the drawbacks of high pass loss and low penetration. Hence, this thesis introduced and verified a mm-wave sigma-delta-over-fiber link architecture with digital beamforming and MU-MIMO functionalities. In this mm-wave link, a QSFP28-based fiber connected the CU with the RRH and supported four sub-channels. A linear array antenna works for the RRH to radiate the mm-wave signal, and communicate with two users, represented by measurement equipment. The demonstration of the digital beamforming function goes up to 700 MSym/s, and the MU-MIMO function has 500 MSym/s for two users.

The thesis proves that D-MIMO has a more uniform and higher capacity than C-MIMO by having more spatial diversity. This thesis also implemented a flexible wideband mm-wave SDoF architecture with digital beamforming and MU-MIMO functionalities suitable for communication networks.

5.2 Future Work

With the future communication system requirement and current technology evolvement, the following topics will be exciting directions to explore.

5.2.1 mm-wave D-MIMO

There are lots of mm-wave single-link studies implemented with high-cost and advanced laboratory equipment. However, those experiments are far from being a real case. An ARoF D-MIMO system has the most complex RRH and is not practical for a massive distributed RHH study. Recently, an SDoF MIMO system works for mm-wave band but suffers from phase noise and lower fiber data rate [70]. This thesis has only studied an mm-wave SDoF link architecture with one RRH, and it can be a building block for the mm-wave D-MIMO system. The fiber connection's high data rate, introduced in this thesis, can have more communication bandwidth than others.

5.2.2 Localization

Future communication networks will be more powerful by having localization functions. With localization functions, the user not only has a communication service but also has localizing service. Previously, the author studied the localization functions with a low-frequency, narrowband SDoF D-MIMO system, and the author proved the theoretical and practical possibilities. The author believes an mm-wave D-MIMO system can significantly improve the localizing accuracy.

References

[1] Ericsson. "Ericsson Mobility Report." Reports and Papers. (Nov. 2022), [Online]. Available: `https://www.ericsson.com/en/reports-and-papers/mobility-report/mobility-visualizer`.

[2] J. G. Andrews, S. Buzzi, W. Choi, S. V. Hanly, A. Lozano, A. C. Soong, and J. C. Zhang, "What Will 5G Be?" *IEEE Journal on selected areas in communications*, vol. 32, no. 6, pp. 1065–1082, 2014.

[3] J. Navarro-Ortiz, P. Romero-Diaz, S. Sendra, P. Ameigeiras, J. J. Ramos-Munoz, and J. M. Lopez-Soler, "A Survey on 5G Usage Scenarios and Traffic Models," *IEEE Communications Surveys Tutorials*, vol. 22, no. 2, pp. 905–929, 2020.

[4] A. Gupta and R. K. Jha, "A Survey of 5G Network: Architecture and Emerging Technologies," *IEEE Access*, vol. 3, pp. 1206–1232, 2015.

[5] M. Jaber, M. A. Imran, R. Tafazolli, and A. Tukmanov, "5G Backhaul Challenges and Emerging Research Directions: A Survey," *IEEE Access*, vol. 4, pp. 1743–1766, 2016.

[6] J. M. Khurpade, D. Rao, and P. D. Sanghavi, "A Survey on IOT and 5G Network," *2018 International Conference on Smart City and Emerging Technology (ICSCET)*, pp. 1–3, 2018.

[7] FAIST. "Distribution of 5G in cities and Countries worldwide." Blog. (Dec. 2022), [Online]. Available: `https://www.faistgroup.com/news/distribution-5g-worldwide/`.

[8] S. A. Abdel Hakeem, H. H. Hussein, and H. Kim, "Vision and research directions of 6g technologies and applications," *Journal of King Saud University - Computer and Information Sciences*, vol. 34, no. 6, Part A, pp. 2419–2442, 2022.

[9] J. Zong, Y. Liu, H. Liu, Q. Wang, and P. Chen, "6G Cell-Free Network Architecture," in *2022 IEEE 2nd International Conference on Electronic Technology, Communication and Information (ICETCI)*, 2022.

[10] Ericsson. "Follow the journey to 6G." 6G. (Dec. 2022), [Online]. Available: `https://www.ericsson.com/en/6g`.

[11] NOKIA Bell Labs. "What is 6G?" Research and Innovation. (Dec. 2022), [Online]. Available: `https://www.bell-labs.com/research-innovation/what-is-6g/`.

[12]   Eindhoven University of Technology. "Center for Wireless Technology Eind-hoven." Research Groups. (Dec. 2022), [Online]. Available: `https://www.tue.nl/en/research/research-groups/center-for-wireless-technology-eindhoven/`.

[13]   University of Oulu. "6G Flagship." (Dec. 2022), [Online]. Available: `https://www.6gflagship.com/`.

[14]   E. G. Larsson, O. Edfors, F. Tufvesson, and T. L. Marzetta, "Massive MIMO for next generation wireless systems," *IEEE Communications Magazine*, vol. 52, no. 2, pp. 186–195, 2014.

[15]   G. Interdonato, E. Björnson, H. Quoc Ngo, P. Frenger, and E. G. Larsson, "Ubiquitous cell-free massive MIMO communications," *EURASIP Journal on Wireless Communications and Networking*, vol. 2019, pp. 1–13, 2019.

[16]   I. C. Sezgin, M. Dahlgren, T. Eriksson, M. Coldrey, C. Larsson, J. Gustavsson, and C. Fager, "A Low-Complexity Distributed-MIMO Testbed Based on High-Speed Sigma–Delta-Over-Fiber," *IEEE Transactions on Microwave Theory and Techniques*, vol. 67, no. 7, pp. 2861–2872, 2019.

[17]   C.-Y. Wu, C. Meysmans, H. Li, J. Van Kerrebrouck, O. Caytan, S. Lemey, J. Bauwelinck, P. Demeester, and G. Torfs, "Demonstration of a Scalable Distributed Antenna System Using Real-Time Bit-Interleaved Sigma-Delta-over-Fiber Architectures," in *2020 European Conference on Optical Communications (ECOC)*, 2020.

[18]   R. Roy, "Spatial division multiple access technology and its application to wireless communication systems," in *1997 IEEE 47th Vehicular Technology Conference. Technology in Motion*, vol. 2, 1997.

[19]   J. Ma, "Modified Shannon's Capacity for Wireless Communication [Speaker's Corner]," *IEEE Microwave Magazine*, vol. 22, no. 9, pp. 97–100, 2021.

[20]   T. L. Marzetta, E. G. Larsson, H. Yang, and H. Q. Ngo, *Fundamentals of Massive MIMO*. Cambridge University Press, 2016.

[21]   R. A. Horn and C. R. Johnson, *Matrix Analysis*, 2nd. USA: Cambridge University Press, 2012.

[22]   S. Kay, *Fundamentals of Statistical Signal Processing: Estimation theory* (Fundamentals of Statistical Signal Processing). Prentice-Hall PTR, 2013.

[23]   T. Brown, P. Kyritsi, and E. De Carvalho, "Capacity of MIMO Channels," in *Practical Guide to MIMO Radio Channel: with MATLAB Examples*. 2009, pp. 17–73.

[24]   E. Björnson, L. Sanguinetti, H. Wymeersch, J. Hoydis, and T. L. Marzetta, "Massive MIMO is a reality—What is next?: Five promising research directions for antenna arrays," *Digital Signal Processing*, vol. 94, pp. 3–20, 2019, Special Issue on Source Localization in Massive MIMO.

[25] E. Björnson, J. Hoydis, and L. Sanguinetti, "Massive MIMO Networks: Spectral, Energy, and Hardware Efficiency," *Foundations and Trends® in Signal Processing*, vol. 11, no. 3-4, pp. 154–655, 2017.

[26] Ö. T. Demir, E. Björnson, and L. Sanguinetti, "Foundations of user-centric cell-free massive MIMO," *Foundations and Trends® in Signal Processing*, vol. 14, no. 3-4, pp. 162–472, 2021.

[27] Business Research Insights. "Radio-over-Fiber market." Market Reports. (Feb. 2023), [Online]. Available: `https://www.businessresearchinsights.com/market-reports/radio-over-fiber-market-100128`.

[28] C. Lim, Y. Tian, C. Ranaweera, T. A. Nirmalathas, E. Wong, and K.-L. Lee, "Evolution of Radio-Over-Fiber Technology," *J. Lightwave Technol.*, vol. 37, no. 6, pp. 1647–1656, 2019.

[29] J. Yuan, Y. Liu, Y. Hu, G. Xu, and J. C. Zhang, "Distributed FD-MIMO (D-FD-MIMO): from Concept to Field Test," in *2022 IEEE Radio and Wireless Symposium (RWS)*, 2022.

[30] A. I. Salama and M. M. Elmesalawy, "Experimental OAI-based Testbed for Evaluating the Impact of Different Functional Splits on C-RAN Performance," in *2019 Novel Intelligent and Leading Emerging Sciences Conference (NILES)*, vol. 1, 2019.

[31] C.-Y. Wu, H. Li, O. Caytan, J. Van Kerrebrouck, L. Breyne, J. Bauwelinck, P. Demeester, and G. Torfs, "Distributed Multi-User MIMO Transmission Using Real-Time Sigma-Delta-Over-Fiber for Next Generation Fronthaul Interface," *Journal of Lightwave Technology*, vol. 38, no. 4, pp. 705–713, 2020.

[32] L. Breyne, G. Torfs, X. Yin, P. Demeester, and J. Bauwelinck, "Comparison Between Analog Radio-Over-Fiber and Sigma Delta Modulated Radio-Over-Fiber," *IEEE Photonics Technology Letters*, vol. 29, no. 21, pp. 1808–1811, 2017.

[33] F. Olofsson, L. Aabel, M. Karlsson, and C. Fager, "Comparison of Transmitter Nonlinearity Impairments in externally modulated Sigma-Delta-over Fiber vs Analog Radio-over-Fiber links," in *2022 Optical Fiber Communications Conference and Exhibition (OFC)*, IEEE, 2022.

[34] I. C. Sezgin, "Sigma-Delta-over-Fiber for High-Speed Wireless Communication Systems," *Chalmers Open Digital Repository*, 2019.

[35] K. Zhu, M. J. Crisp, S. He, R. V. Penty, and I. H. White, "MIMO System Capacity Improvements Using Radio-over-Fibre Distributed Antenna System Technology," in *2011 Optical Fiber Communication Conference and Exposition and the National Fiber Optic Engineers Conference*, 2011.

[36] A. Shaikh and M. J. Kaur, "Comprehensive Survey of Massive MIMO for 5G Communications," in *2019 Advances in Science and Engineering Technology International Conferences (ASET)*, 2019.

[37] J. Vieira, S. Malkowsky, K. Nieman, Z. Miers, N. Kundargi, L. Liu, I. Wong, V. Öwall, O. Edfors, and F. Tufvesson, "A flexible 100-antenna testbed for Massive MIMO," in *2014 IEEE Globecom Workshops (GC Wkshps)*, 2014.

[38] S. Malkowsky, J. Vieira, L. Liu, P. Harris, K. Nieman, N. Kundargi, I. C. Wong, F. Tufvesson, V. Öwall, and O. Edfors, "The World's First Real-Time Testbed for Massive MIMO: Design, Implementation, and Validation," *IEEE Access*, vol. 5, pp. 9073–9088, 2017.

[39] P. Harris, S. Malkowsky, J. Vieira, E. Bengtsson, F. Tufvesson, W. B. Hasan, L. Liu, M. Beach, S. Armour, and O. Edfors, "Performance Characterization of a Real-Time Massive MIMO System With LOS Mobile Channels," *IEEE Journal on Selected Areas in Communications*, vol. 35, no. 6, pp. 1244–1253, 2017.

[40] X. Jiang and F. Kaltenberger, "Demo: an LTE compatible massive MIMO testbed based on OpenAirInterface," in *WSA 2017; 21th International ITG Workshop on Smart Antennas*, 2017.

[41] G. Xu, Y. Li, J. Yuan, R. Monroe, S. Rajagopal, S. Ramakrishna, Y. H. Nam, J.-Y. Seol, J. Kim, M. M. U. Gul, A. Aziz, and J. Zhang, "Full Dimension MIMO (FD-MIMO): Demonstrating Commercial Feasibility," *IEEE Journal on Selected Areas in Communications*, vol. 35, no. 8, pp. 1876–1886, 2017.

[42] Ericsson. "Ericsson Massive MIMO." RAN. (Dec. 2022), [Online]. Available: `http://www-cs-faculty.stanford.edu/~uno/abcde.html`.

[43] P. von Butovitsch, D. Astely, C. Friberg, A. Furuskär, B. Göransson, B. Hogan, J. Karlsson, and E. Larsson, "Advanced antenna systems for 5G networks," *Ericsson White Paper*, 2018.

[44] GlobeNewswire. "Nokia and Sprint demonstrate massive MIMO at MWC17." Source: Nokia Oyj. (Dec. 2022), [Online]. Available: `https://www.globenewswire.com/news-release/2017/02/27/927989/0/en/Nokia-and-Sprint-demonstrate-massive-MIMO-at-MWC17.html`.

[45] A. P. Guevara, C.-M. Chen, and S. Pollin, "Hardware and Spectrum Sharing for Distributed Massive MIMO," in *2018 52nd Asilomar Conference on Signals, Systems, and Computers*, 2018.

[46] C.-M. Chen, V. Volski, L. Van der Perre, G. A. E. Vandenbosch, and S. Pollin, "Finite Large Antenna Arrays for Massive MIMO: Characterization and System Impact," *IEEE Transactions on Antennas and Propagation*, vol. 65, no. 12, pp. 6712–6720, 2017.

[47] C.-M. Chen, Q. Wang, A. Gaber, A. P. Guevara, and S. Pollin, "Experimental Study of User Selection for Dense Indoor Massive MIMO," in *IEEE INFOCOM 2019 - IEEE Conference on Computer Communications Workshops (INFOCOM WKSHPS)*, 2019.

[48] L. Van der Perre, E. G. Larsson, F. Tufvesson, L. D. Strycker, E. Björnson, and O. Edfors, "RadioWeaves for efficient connectivity: analysis and impact of constraints in actual deployments," in *2019 53rd Asilomar Conference on Signals, Systems, and Computers*, 2019.

[49] A. P. Guevara, S. De Bast, and S. Pollin, "Weave and Conquer: A Measurement-based Analysis of Dense Antenna Deployments," in *ICC 2021 - IEEE International Conference on Communications*, 2021.

[50] Ericsson. "Radio Stripes: re-thinking mobile networks." Ericsson Blog. (Feb. 2019), [Online]. Available: https://www.ericsson.com/en/blog/2019/2/radio-stripes.

[51] H. Q. Ngo, A. Ashikhmin, H. Yang, E. G. Larsson, and T. L. Marzetta, "Cell-Free Massive MIMO Versus Small Cells," *IEEE Transactions on Wireless Communications*, vol. 16, no. 3, pp. 1834–1850, 2017.

[52] Z. Liu and L. Dai, "Asymptotic capacity analysis of downlink MIMO systems with co-located and distributed antennas," in *2013 IEEE 24th Annual International Symposium on Personal, Indoor, and Mobile Radio Communications (PIMRC)*, IEEE, 2013.

[53] M. K. Bhatt, B. S. Sedani, K. R. Parmar, and M. P. Shah, "Ergodic UL/DL capacity analysis of co-located and distributed antenna configuration for high speed train with massive MIMO system," in *2017 International Conference on Inventive Computing and Informatics (ICICI)*, 2017.

[54] R. Ibernon-Fernandez, J.-M. Molina-Garcia-Pardo, and L. Juan-Llacer, "Comparison Between Measurements and Simulations of Conventional and Distributed MIMO System," *IEEE Antennas and Wireless Propagation Letters*, vol. 7, pp. 546–549, 2008.

[55] E. Rådahl and S. Rimborg, "Simulations of the Capacity and Coverage for a Multi-User Distributed MIMO Network," *Chalmers Open Digital Repository*, 2021.

[56] L. Xiao, L. Dai, H. Zhuang, S. Zhou, and Y. Yao, "Information-theoretic capacity analysis in MIMO distributed antenna systems," in *The 57th IEEE Semiannual Vehicular Technology Conference, 2003. VTC 2003-Spring.*, vol. 1, 2003.

[57] Ettus. "USRP B205mini-i." USRP Bus Series. (Nov. 2022), [Online]. Available: https://www.ettus.com/all-products/usrp-b205mini-i.

[58] B. Vucetic and J. Yuan, *Space-time coding.* John Wiley & Sons, 2003.

[59] Remcom. "InSite." Wireless InSite EM propagation software. (Nov. 2022), [Online]. Available: https://www.remcom.com/wireless-insite-em-propagation-software.

[60] D. Konstantinou, T. A. Bressner, S. Rommel, U. Johannsen, M. N. Johansson, M. V. Ivashina, A. B. Smolders, and I. T. Monroy, "5G RAN architecture based on analog radio-over-fiber fronthaul over UDWDM-PON and phased array fed reflector antennas," *Optics Communications*, vol. 454, p. 124 464, 2020.

[61] A. H. M. R. Islam, M. Bakaul, and A. Nirmalathas, "Multilevel Modulations for Gigabit Access in a Simple Millimeter-Wave Radio-Over-Fiber Link," *IEEE Photonics Technology Letters*, vol. 24, no. 20, pp. 1860–1863, 2012.

[62] L. Bogaert, J. Van Kerrebrouck, H. Li, I. L. de Paula, K. Van Gasse, C.-Y. Wu, P. Ossieur, S. Lemey, H. Rogier, P. Demeester, G. Roelkens, J. Bauwelinck, and G. Torfs, "SiPhotonics/GaAs 28-GHz Transceiver With Reflective EAM for Laser-Less mmWave-Over-Fiber," *Journal of Lightwave Technology*, vol. 39, no. 3, pp. 779–786, 2021.

[63] R. Budé, M. M. Versluis, G. Nazarikov, S. Rommel, B. van Ark, U. Johannsen, I. T. Monroy, and A. B. Smolders, "Millimeter-Wave Outphasing using Analog-Radio over Fiber for 5G Physical Layer Infrastructure," in *2020 50th European Microwave Conference (EuMC)*, 2021.

[64] R. Puerta, J. Yu, X. Li, Y. Xu, J. J. Vegas Olmos, and I. Tafur Monroy, "Single-Carrier Dual-Polarization 328-Gb/s Wireless Transmission in a D-Band Millimeter Wave 2 × 2 MU-MIMO Radio-Over-Fiber System," *Journal of Lightwave Technology*, vol. 36, no. 2, pp. 587–593, 2018.

[65] M. Sung, J. Kim, E.-S. Kim, S.-H. Cho, Y.-J. Won, B.-C. Lim, S.-Y. Pyun, J. K. Lee, and J. H. Lee, "Demonstration of 5G Trial Service in 28 GHz Millimeter Wave using IFoF-Based Analog Distributed Antenna System," in *2019 Optical Fiber Communications Conference and Exhibition (OFC)*, 2019.

[66] T. Nagayama, S. Akiba, T. Tomura, and J. Hirokawa, "Photonics-Based Millimeter-Wave Band Remote Beamforming of Array-Antenna Integrated With Photodiode Using Variable Optical Delay Line and Attenuator," *Journal of Lightwave Technology*, vol. 36, no. 19, pp. 4416–4422, 2018.

[67] M. Morant, A. Trinidad, E. Tangdiongga, T. Koonen, and R. Llorente, "Multi-Beamforming Provided by Dual-Wavelength True Time Delay PIC and Multi-core Fiber," *Journal of Lightwave Technology*, vol. 38, no. 19, pp. 5311–5317, 2020.

[68] I. Lima de Paula, L. Bogaert, O. Caytan, J. Van Kerrebrouck, A. Moerman, M. Muneeb, Q. V. d. Brande, G. Torfs, J. Bauwelinck, H. Rogier, P. Demeester, G. Roelkens, and S. Lemey, "Air-Filled SIW Remote Antenna Unit With True Time Delay Optical Beamforming for mmWave-Over-Fiber Systems," *Journal of Lightwave Technology*, vol. 40, no. 20, pp. 6961–6975, 2022.

[69] K. Ito, M. Suga, T. Arai, Y. Shirato, N. Kita, and T. Onizawa, "Passive beamformer based remote beamforming scheme for radio-over-fiber systems: Experimental demonstration using 28-GHz band reflectarray," *Optics Communications*, vol. 513, p. 128 026, 2022.

[70] C.-Y. Wu, H. Li, J. Van Kerrebrouck, A. Vandierendonck, I. L. de Paula, L. Breyne, O. Caytan, S. Lemey, H. Rogier, J. Bauwelinck, P. Demeester, and G. Torfs, "Distributed Antenna System Using Sigma-Delta Intermediate-Frequency-Over-Fiber for Frequency Bands Above 24 GHz," *Journal of Lightwave Technology*, vol. 38, no. 10, pp. 2765–2773, 2020.

[71] H. Li, M. Verplaetse, J. Verbist, J. Van Kerrebrouck, L. Breyne, C.-Y. Wu, L. Bogaert, B. Moeneclaey, X. Yin, J. Bauwelinck, P. Demeester, and G. Torfs, "Real-Time 100-GS/s Sigma-Delta Modulator for All-Digital Radio-Over-Fiber Transmission," *Journal of Lightwave Technology*, vol. 38, no. 2, pp. 386–393, 2020.

[72] R. Schreier and G. C. Temes, *Understanding Delta-Sigma Data Converters.* Piscataway, NJ: IEEE press, 2005, vol. 74.

[73] Keysight. "N9042B UXA X-Series Signal Analyzer." Products. (Nov. 2022), [Online]. Available: https://www.keysight.com/it/en/product/N9042B/uxa-signal-analyzer-2-hz-50-ghz.html.

[74] Xilinx, Inc. "Virtex UltraScale+ HBM VCU128 FPGA Evaluation Kit." Boards and Kits. (Nov. 2022), [Online]. Available: https://www.xilinx.com/products/boards-and-kits/vcu128.html.

[75] FS. "Cisco QSFP-100G-SR4-S Compatible 100GBASE-SR4 QSFP28 850nm 100m DOM MTP/MPO-12 MMF Optical Transceiver Module." products. (Nov. 2022), [Online]. Available: https://www.fs.com/de-en/products/48354.html?attribute=12780&id=566810.

[76] Mini-Circuits. "ZX10Q-2-27+." RF & Microwave Products. (Nov. 2022), [Online]. Available: https://www.minicircuits.com/pdfs/ZX10Q-2-27+.pdf.

[77] Mini-Circuits. "ZX10R-14-S+." RF & Microwave Products. (Nov. 2022), [Online]. Available: https://www.minicircuits.com/pdfs/ZX10R-14-S+.pdf.

[78] Analog Devices. "24 GHz to 44 GHz, Wideband, Microwave Upconverter." ADMV1013. (Nov. 2022), [Online]. Available: https://www.analog.com/media/en/technical-documentation/data-sheets/ADMV1013.pdf.

[79] 3GPP, *Evolved Universal Terrestrial Radio Access (E-UTRA); Base Station (BS) radio transmission and reception (release 16) (V16.3.0)*, TS 36.104, TS 36.104, 2019.

[80] T. Ingason and H. Liu, "Line-of-Sight MIMO for Microwave Links-Adaptive Dual Polarized and Spatially Separated Systems," M.S. thesis, Chalmers University of Technology, 2009.

[81] M. Sung, J. Kim, E.-S. Kim, S.-H. Cho, Y.-J. Won, B.-C. Lim, S.-Y. Pyun, H. Lee, J. K. Lee, and J. H. Lee, "RoF-Based Radio Access Network for 5G Mobile Communication Systems in 28 GHz Millimeter-Wave," *Journal of Lightwave Technology*, vol. 38, no. 2, pp. 409–420, 2020.

[82] A. Moerman, J. Van Kerrebrouck, O. Caytan, I. L. de Paula, L. Bogaert, G. Torfs, P. Demeester, M. Moeneclaey, H. Rogier, and S. Lemey, "mmWave-over-Fiber Distributed Antenna Systems for Reliable multi-Gbps Wireless Communication," in *2022 3rd URSI Atlantic and Asia Pacific Radio Science Meeting (AT-AP-RASC)*, 2022.

[83] R. A. Shafik, M. S. Rahman, and A. R. Islam, "On the Extended Relationships Among EVM, BER and SNR as Performance Metrics," in *2006 International Conference on Electrical and Computer Engineering*, 2006.